Universidade de Aveiro Departmento de Física
Ano 2010

DERESE GUGSA DESTA

ESTUDO DE CÉLULAS SOLARES HÍBRIDAS DE Si-NC/P3HT FABRICADAS EM AMBIENTE ATMOSFÉRICO

STUDY OF AIR-PROCESSED Si-NC/P3HT HYBRID SOLAR CELLS

Universidade de Aveiro Departmento de Física
Ano 2010

DERESE GUGSA DESTA

ESTUDO DE CÉLULAS SOLARES HÍBRIDAS DE Si-NC/P3HT FABRICADAS EM AMBIENTE ATMOSFÉRICO

STUDY OF AIR-PROCESSED Si-NC/P3HT HYBRID SOLAR CELLS

A dissertation presented to the University of Aveiro to fulfill the formalities essential to obtain the Master degree in Materials Science (Erasmus Mundus), carried out under the scientific supervision of Dr. Rui N. Pereira and Dr. António F. da Cunha, Department of Physics, University of Aveiro**.**

Dissertação apresentada à Universidade de Aveiro para cumprimento as formalidades essenciais à obtenção do grau de Mestre em Ciência dos Materiais (Erasmus Mundus), realizado, sob a supervisão científica do Dr. N. Rui Pereira e do Dr. António F. da Cunha, Departamento de Física, Universidade de Aveiro.

O júri

Presidente Professor Vítor Brás de Sequeira Amaral
Professor catedrático Universidade de Aveiro

Doutora Maria João de Sousa Brites
Investgadora auxiliar do Laboratório Nacional de Energia e Geologia

Vogais Doutor António Ferreira da Cunha
Professor auxiliar da Universidade de Aveiro

Doutor Rui Nuno Marques Pereira
Investigador do Departmento de Física da Universidade de Aveiro

Acknowledgement I am heartily thankful to my supervisors, Dr. Rui N. Pereira, Researcher at the University of Aveiro, and Dr. António F da Cunha, Assistant Professor at the University of Aveiro for their invaluable guidance, advice and constructive comments throughout the work. I gratefully acknowledge Dr. Rui N. Pereira for his crucial contribution that gave me extraordinary experience throughout the work. I also would like to thank Dr. Ana Barros for her supervision and constructive comments.

My special gratitude also goes to Dr. Edison Pecoraro, Researcher at the institute of telecommunications, for his invaluable suggestions and help in preparing necessary experimental setups. I also would like to thank Marta Ferro for her help in acquiring SEM images. Lastly, I offer my regards and blessings to all those who helped me in all aspects of the thesis work.

I would like to extend my special thanks to the European Commission for funding my Master study through Erasmus Mundus scholarship scheme.

Palavras-chave Heterojunção maioria, células solares híbridas fabricadas em ambiente atmosphérico, eficiência de conversão do poder, EPR

Resumo Neste trabalho são estudadas células solares híbridas formadas por poli(3-hexiltiofeno-2,5-diyl) (P3HT) como condutor orgânico de buracos e nanocristais de silício (Si-NCs) como conductor de electrões inorgânico. Células solares híbridas têm atraído muita atenção nos últimos anos devido ao facto de serem potencialmente fabricadas a baixo custo, a sua flexibilidade e baixo peso. As possibilidades de processamento em solução e ajuste da região espectral de absorção, a baixa toxicidade, e a abundância fazem dos Si-NCs um material atractivo para aplicação em células solares. Si-NCs de elevada qualidade podem hoje em dia ser produzidos em larga escala a partir da fase gasosa através da decomposição de silano num plasma. Embora a superfícies destes Si-NCs seja terminada com ligações Si-H durante a sua síntese, estes desenvolvem uma camada de óxido na superfície quando são expostos ao ar. Até agora, células híbridas de Si-NC/P3HT foram fabricadas com Si-NCs que não foram expostos ao ar após a sua síntese e foram posteriormente estudadas em condições de atmosfera inerte, devido à expectativa de que a exposição ao ar resulta na sua degradação. No entanto, o processamento de dispositivos em atmosfera inerte impõe limitações em termos técnicos e custo. Nesta tese estudamos o efeito do processamento em atmosfera de ar na performance e degradação de células solares híbridas de Si-NC/P3HT. As células foram fabricadas em ar e em atmosfera de azoto e caracterizadas à temperatura ambiente e condições de exposição ao ar. Para produzir a células solares foram usados Si-NCs que foram expostos ao ar após a síntese e que por isso contêm uma camada de óxido na sua superfície. Para remover esta camada, nós usamos um método de erosão química com uma solução diluída de ácido hidroflurico (HF). Células solares fabricadas com uma mistura de 1:1 em percentagem de peso (wt.%) de Si-NC:P3HT não revelaram qualquer efeito fotovoltaico. Dispositivos fabricados com uma

mistura de 2:1 wt.% de Si-NC:P3HT mostraram efeito fotovoltaico, devido à formação de uma rede interpenetrara de Si-NC e P3HT em toda a extensão do filme foto activo, tal como revelado em imagens de microscopia electrónica de varrimento. Dispositivos fabricados em atmosfera inerte não revelaram uma performance melhorada em relação aos dispositivos produzido em atmosfera de ar, indicando que a fabricação das células solares em ar não é o factor determinante da performance das nossas células solares. Células solares que mostraram um efeitos fotovoltaico degradaram-se rapidamente por exposição ao ar. Em contrate, filmes de P3HT e de misturas Si-NC/P3HT, estudados em experiências separadas, não revelaram uma degradação significativa por exposição ao ar. Estes resultados indicma que a degradação das células solares não deve resultar da degradação da camada foto activa de Si-NC/P3HT, mas poderá resultar da degradação de interfaces entre as varias camadas que compõem as células. Medidas de ressonância paramagnética electrónica (RPE) foram levadas a cabo com os Si-NCs usados nas nossas células e com Si-NCs usados para fabricar as células estudadas em trabalhos publicados anteriormente por outros grupos. Estas medidas revelaram que o número de defeitos superficiais por nanocristal nos nossos Si-NCs é cerca de três ordens de grandeza superior ao número encontrado nos Si-NCs usados anteriormente. Este facto poderá explicar a baixa performance fotovoltaica os nossos dispositivos.

Key Words Bulk heterojunction, air-processed hybrid solar cells, degradation, power conversion efficiency, EPR

Abstract We study-air-processed organic-inorganic hybrid solar cells, which incorporate poly(3-hexylthiophene-2,5-diyl) (P3HT) as organic hole conductor and silicon nanocrystals (Si-NCs) as inorganic electron conductor. Hybrid solar cells have received a lot of attention in recent years due to their low cost, flexibility and lightweight. Solution processability, non-toxicity, abundance and tunable absorption spectral range of Si-NCs make them attractive materials for application in solar cells. High quality Si-NCs can now a days be produced in large amounts from the gas phase decomposition of silane in a plasma. Although the surface of these Si-NCs is terminated with Si-H bonds immediately after synthesis, they develop an insulating native oxide shell after being exposed to air. So far, Si-NC/P3HT hybrid solar cells have only been fabricated using Si-NCs that have not been exposed to air after synthesis and afterwards characterized under inert atmosphere conditions due to the expectation that air exposure of the devices leads to their degradation. However, inert atmosphere processing has some technical and cost efficiency limitations. In this thesis, we study the effect of air-processing on the performance and degradation of solar cells based on Si-NC/P3HT. Hybrid solar cells were fabricated in air and under nitrogen ambient and characterized at room temperature under atmospheric air. To produce our solar cells we use Si-NCs that have been stored in air after plasma synthesis and, therefore, contain a native oxide at their surface. To remove this oxide layer we apply wet etching with a dilute hydrofluoric acid (HF) solution. Solar cells made from 1:1 wt.% (HF-etched Si-NC:P3HT) composition did not show detectable photovoltaic effect. A very small photovoltaic effect has been observed for devices made from 2:1 wt.% (HF-etched Si-NC:P3HT) composition as a result of the formation of an interpenetrated network throughout the photoactive film at higher NC concentration as seen from scanning electron microscopy. Device fabrication under inert atmosphere did not result in improved solar cell performance. This shows that fabrication of the devices in air was not the main reason for the poor performance of the hybrid solar cells. Moreover,

solar cells that exhibited a photovoltaic effect were found to degrade within one day of air exposure. In contrast to this, the conductivity of P3HT, (unetched Si-NC)/P3HT and (HF-etched Si-NC)/P3HT films, studied in separate experiments, did not show significant degradation upon air exposure. These results indicate that the degradation of the solar cells is not due to degradation of individual photoactive layers, but could rather originate from degradation of interfaces between the different layers. Electron paramagnetic resonance measurements carried out with our Si-NCs and with Si-NCs used in previous investigations of Si-NC/P3HT solar cells revealed that the number of surface defects per NC is about three orders of magnitude larger in our NCs than in those used in the previous investigations. This could be a reason for the poor performance of our Si-NC/P3HT hybrid solar cells.

Acronyms and Abbreviations

AM	Air mass
BHJ SC	Bulk heterojunction solar cell
CB	Conduction band
DSSC	Dye sensitized solar cell
EPR	Electron paramagnetic resonance
FTIR	Fourier transform infrared
HH	Head to head
HOMO	Highest occupied molecular orbital
HT	Head to tail
IPCE	Incident photon to current efficiency
ITO	Indium tin oxide
LUMO	Lowest unoccupied molecular orbital
MEH-PPV	Poly[2-methoxy 5-(2'-ethyl-hexyloxy)-p-phenylenevinylene]
MeO	Metal oxide
P3AT	Poly(3-alkylthiophene)
P3HT	Poly(3-hexylthiophene)
PCE	Power conversion efficiency
PDDTT	Poly[5,7-bis(4-decanyl-2-thienyl)thieno[3,4-b]diathiazole-thiophene-2,5)]
PEDOT:PSS	Poly(3, 4-ethylene dioxythiophene):poly(styrene sulfonate)
PPTTT	Poly[2,5-bis (3-alkylthiophene-2-yl)thieno[3,2-b]thiophene]
PTAA	Poly(triarylamine)
PTFE	polytetrafluoroethylene
PTV	Poly(thienylene vinylene)
PV	Photovoltaic
PVDF	Polyvinylidene fluoride
rpm	revolutions per minute
SEM	Scanning electron microscope
Si-NCs	Silicon nanocrystals
TCO	Transparent conductive oxide
TT	Tail to tail
UV-visible	Ultraviolet- visible
VB	Valence Band

Table of Contents

List of Figures

List of Tables

1. Introduction

1.1 Necessity of alternative energy sources

The change in civilization life with energy resources and growth of world population at high rate increased the present energy consumption to a much high level [1]. Despite the limited supply of today's main energy sources such as coal, oil, and natural gas, the release of greenhouse gases as a result of their combustion created an unprecedented environmental effect. Hence, the need of renewable and environmentally friendly energy sources is unquestionable. It is estimated that the worldwide energy supply in recent years is in the order of 20 TW, which is about four orders of magnitude less than the energy that the sun radiates to the earth (about 10^5 TW) [2]. Hence, currently there is a very high need to replace the traditional energy sources with renewable energy sources, such as solar energy, wind energy, geothermal energy, and hydropower [1]. As a result, solar energy that converts light into electrical energy has been a great scientific issue in the present years. However, the cost of traditional photovoltaic (PV) modules, which demand extensive processing techniques and high materials purity, are unaffordable to be used as a common energy source. Despite the decrement of the cost of PV modules due to the advancement in current processing technologies, it is still expensive and has reached at a point where further price decrement is difficult, as crystalline silicon is too expensive. Under AM 1.5 illumination, power conversion efficiencies (PCE) higher than 20 % have been reported for silicon and GaAs based photovoltaic (PV) cells despite their production cost and energy consumption during the fabrication process [3]. This superior efficiency of inorganic solar cells was mainly attributed to the reduced recombination losses as a result of the high intrinsic charge carrier mobilities that exist in inorganic semiconductors.

Recently, organic-inorganic hybrid photovoltaic cells are among a hot topic of investigations due to their promising features such as low fabrication cost, flexibility, and lightweight [4]. Furthermore, solution processability, high hole mobility and strong visible absorption properties of conjugated polymers can be

combined with high electron mobility, high electron affinity and tunable optical properties of semiconducting nanocrystals to overcome the low power conversion efficiency of organic solar cells [4]. The main factors attributed to the low power conversion efficiency of organic solar cells are low carrier mobility, lack of absorption in the red/near infrared (NIR) part of the spectrum, poor environmental stability and excitonic character of photocarrier generation [5]. The binding energy of excitons is in the order of 0.1 eV, hence room temperature thermal excitation (25 meV) is too small to create free charge carriers [5]. Thus, it is necessary to select two materials with sufficient electron affinity differences, such that the electron goes to the material with high electron affinity and the hole goes to the material with low electron affinity after being dissociated at the donor/acceptor interface. The exciton diffusion length is small for organic semiconductors, around 10 nm for poly(3-hexylthiophene) (P3HT); as a result nanoscale phase separation must be achieved between the active organic and inorganic semiconductors, that must be within the exciton diffusion length, otherwise the charge carriers will recombine before reaching to the donor/acceptor interface [5]. In addition to this, to collect the charge carriers at the respective electrodes there must be an electrically continuous path from the interface where the charge carriers are generated to the electrodes. If the size of organic/or inorganic domain is too small, it will be difficult to form continuous conduction path and hence the charge collection efficiency will decrease. On the other hand, if the domain sizes are too large, excitons will not be able to reach at the donor/acceptor interface limiting the performance of hybrid solar cells. Therefore, to achieve a solar cell with good power conversion efficiency, it is necessary to control the domain size.

Hybrid solar cells based on blends of poly(3-hexylthiophene) (P3HT) and CdSe nanocrystals have been reported to have high power conversion efficiency (PCE > 2%) [6] compared to other hybrid solar cells reported so far. Hybrid solar cells made using ZnO [7] and TiO_2 [8] nanocrystals as electron transporting materials are reported to have remarkable efficiencies, but due to their wide bandgap they have poor visible absorption, as a result their performance is limited [9]. The use of silicon nanocrystals (Si-NCs) for

photovoltaic applications may be beneficiary from many aspects, such as, its non-toxicity, abundance, strong UV absorption and possibility of multiple exciton generation [9]. Moreover, the possibility of fabricating Si-NCs at a very high yield using low pressure microwave plasma reactor made them attractive material for solar cell applications [9]. In conjunction with Si-NCs, poly(3-hexylthiophene) (P3HT) has been used due to its suitable energy alignment with Si-NCs, which is beneficial for the dissociation of excitons at the interface and its high absorption coefficient in the visible spectral range [9]. Lui *et al.* recently fabricated hybrid solar cells from P3HT and Si-NCs and studied the effect of Si-NC size and weight ratio on the performance of the hybrid solar cells [9]. Under simulated one-sun AM 1.5 direct illumination (100 mW/cm^2), they reported the best power conversion efficiency (1.15 %) for devices made from Si-NCs having size 3-5 nm at 35 wt.% [9]. These devices have though been fabricated under conditions of O_2 and H_2O exclusion, which is technically problematic and costly.

1.2 Objectives and structure of this thesis

All hybrid solar cells reported so far are fabricated and characterized under inert atmosphere in a glove box. To the best of our knowledge the effect of device fabrication in air on the performance of hybrid solar cells was not fully investigated. The objective of this thesis is to investigate the effect of air processing on the performance of Si-NC/P3HT hybrid solar cells. We will relate the performance of the hybrid solar cells with the morphology of the photoactive film and finally we will investigate air degradation of the hybrid devices, and compare it with the behavior of P3HT film and Si-NC/P3HT film upon exposure to air.

This thesis is organized into five sections: Introduction, Literature review, Experiments, Experimental data and discussion, and Conclusions. In the Literature review part operating principle and architecture of solar cells is outlined, and then organic/inorganic hybrid solar cells and potential of Si-NCs and P3HT for solar cell application are discussed. In the Experimental section characterization conditions of our experiments are briefly described. In the section Experimental data and discussion UV-visible, FTIR and conductivity

data of Si-NCs, P3HT and Si-NC/P3HT films are presented and discussed. Moreover, the current-voltage characteristics of Si-NC/P3HT hybrid solar cells are discussed. Then, results of electron paramagnetic resonance measurement are shown. Finally, the conclusion and future direction are presented.

2. Literature Review

2.1 Architecture and principle of operation of organic solar cells

In organic solar cells, indium tin oxide (ITO) coated glass substrate is commonly used as anode due its transparency to light and commercial availability. On top of ITO, a thin layer of PEDOT:PSS is deposited to facilitate hole transport, to block electrons from reaching to the ITO layer, and to prevent the diffusion of materials from the ITO layer to the photoactive layer [10]. Then, a photoactive layer is deposited on top of PEDOT:PSS layer. The main light absorbers in organic solar cells are organic semiconductors hence, absorption of light leads to the generation of bound electron-hole pairs called excitons. To have useful electrical current, excitons should diffuse to the donor/acceptor interface where they get dissociated into holes and electrons and migrate through the photoactive layer towards their respective electrodes. Finally, aluminum contact has been deposited as cathode.

The first organic solar cell was demonstrated through asymmetrical device configuration, where a single photoactive layer is sandwiched between two dissimilar electrodes [10]. One of the big challenges in organic photovoltaics is to dissociate photo generated excitons into electrons and holes and transfer these charge carriers out of the solar cell so that they can contribute to an electrical current. In a single photoactive layer device, the built-in potential needed to migrate free charge carriers towards their respective electrodes is derived either from the difference in work function of the two electrodes or from the Schottky type potential barrier at one of the organic/metal contact [10]. The large series resistance associated with insulating nature of the organic layer and field dependent generation of charge carriers in organic photoconductors were considered to be responsible for the low power conversion efficiency of such devices [10]. Hence, the main drawback of this configuration was that, only excitons generated near to the electrodes will dissociate and contribute to the photocurrent. This limitation was later overcome by using donor-acceptor heterojunction, where the excitons generated will dissociate at the

donor/acceptor interface and the resulting free charge carriers will transport through the respective donor and acceptor material to be collected at the electrodes [10]. It was found that the time scale of photo-induced charge separation at the donor (organic polymer)/acceptor (C60) interface was nearly 10^3 faster than non-radiative decay of photo-excitations [10]. This lead to the conclusion that replacing the single photoactive layer in conventional organic solar cells with a heterojunction layer can enhance the quantum efficiency of charge separation close to unity.

Depending on their configuration, organic heterojunction photovoltaic devices can be grouped into two categories bilayer heterojunction solar cells and bulk heterojunction solar cells (BHJ SCs). In bilayer heterojunction photovoltaic cells the junction between the donor and acceptor is planar, Figure 2.1 (a). As a result efficient separation of charge carriers can only occur at the donor/acceptor plane interface. This means that excitons that are generated far from the donor/acceptor junction will recombine before reaching the heterojunction. On the other hand, in bulk heterojunction solar cells the photoactive layer was made by blending donor and acceptor materials, Figure 2.1 (b). Bulk heterojunction (BHJ) is formed by interpenetrating donor/acceptor networks that are separated from each other at nanometeric scale forming a bi-continuous donor/acceptor material. Hence, the separation of photo-induced charge carriers in BHJ SCs occurs throughout the photoactive layer overcoming the limitation of bilayer heterojunction devices.

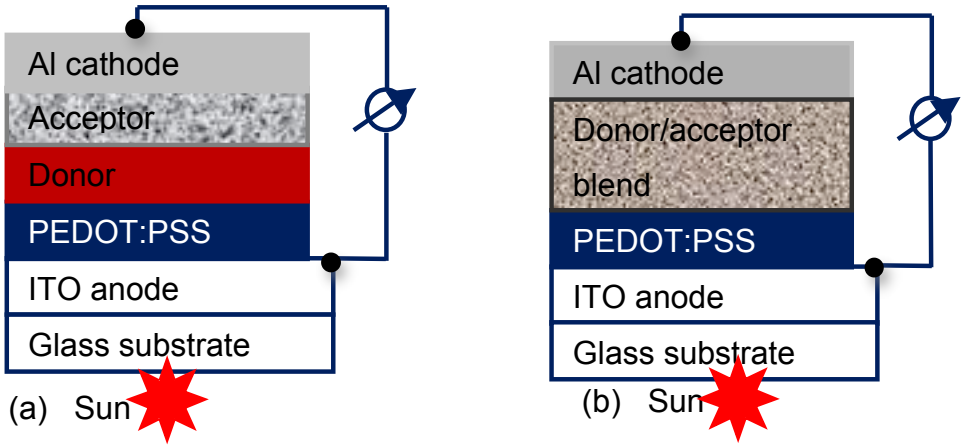

Figure 2.1: Schematic layout of a) bilayer photovoltaic cell and b) bulk heterojunction photovoltaic cell.

Thus, in the bulk heterojunction device the interface between the phases is maximized, so that excitons will be efficiently dissociated. In both configurations, the photo-generated current at the interface was found to be weakly dependent on the bias field. This overcomes the serious limitation of single layer organic solar cells providing high fill factor. Moreover, the nature of the interface at the heterojunction dictates both the magnitude and polarity of the open circuit voltage [10].

In organic solar cells, optical absorption in conjugated polymers excites an electron from HOMO to LUMO of the donor material, leaving a hole behind, as shown in Figure 2.2. The electron-hole pair, also called exciton, will diffuse towards the donor/acceptor interface and gets dissociated. Then, the electron will be transferred to the LUMO of the acceptor which has a lower lying conduction band and migrate to the cathode, while holes transport to the anode. Both exciton dissociation and electron collection efficiency strongly depend on the morphology of the photoactive layer. Since the diffusion length of excitons in conjugated polymers is very small (about 10 nm), the phase separation between the donor and acceptor material must be in the order of a few nanometers. Moreover, there has to be electrically conductive paths for both charge carriers to collect them at their respective electrodes.

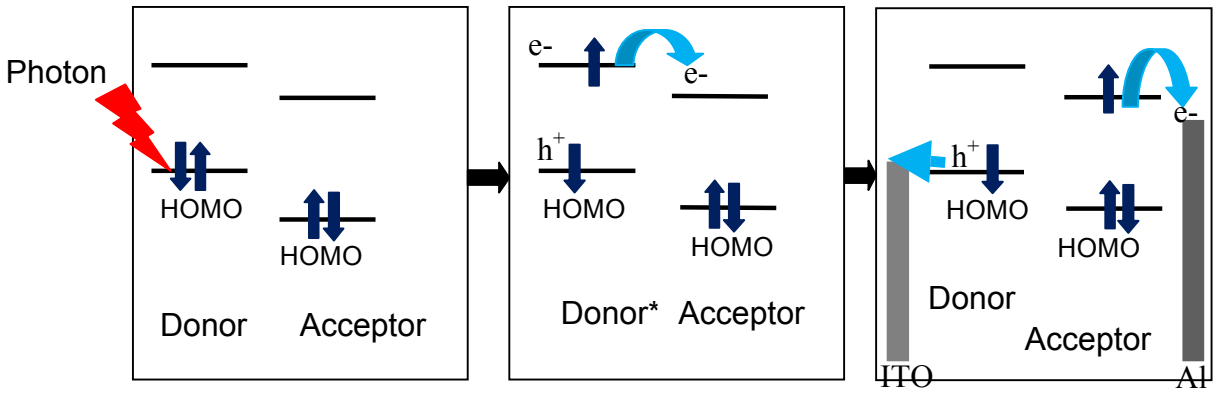

Figure 2.2: Energy scheme illustrating the working principle of an organic photovoltaic (PV) device. Illumination results in generation of excitons, which separate at the donor/acceptor interface, followed by migration of photo generated charge carriers to their respective electrodes.

2.2 Hybrid solar cells

Hybrid solar cells formed by incorporating both inorganic semiconductor nanocrystals and organic semiconductors combine the benefits from both classes of materials. The absorbance of nanocrystals can be tuned by materials selection and quantum confinement; moreover their shape and size can be controlled to optimize the performance of photovoltaic devices. These advantages of nanocrystals could be combined with the high absorption coefficient of organic semiconductors retaining solution processability of the organic/ inorganic blend. Figure 2.3 shows a simple classification of hybrid solar cells.

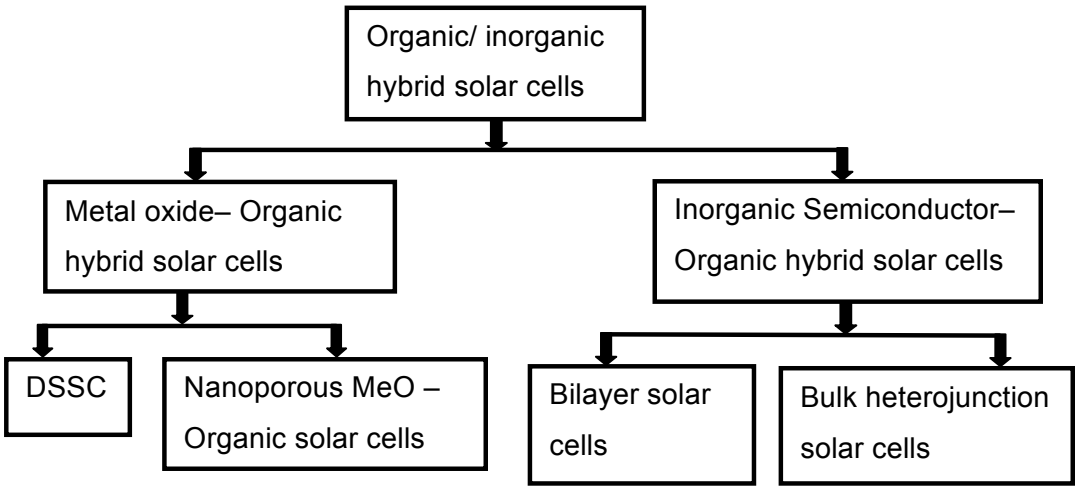

Figure 2.3: Classification of Hybrid solar cells

2.2.1 Metal oxide (MeO)– organic hybrid solar cells

2.2.1.1 Dye sensitized and nanoporous MeO solar cells

Dye sensitized solar cell (DSSC) based on nanocrystalline TiO_2 was demonstrated for the first time in 1991 by O'Regan and Gratzel [11]. The reported efficiency of this solar cell was 7.1 %. Nanoporous TiO_2 electrode was used to maximize the interfacial area between the dye and electrode resulting a tremendous increase in photoreaction area [12]. Power conversion efficiencies over 10 % have been reported in recent years upon careful control of the morphology of the porous nanostructured TiO_2 film and appropriate choice of organic dyes [11]. Dye sensitized solar cells are composed of dye sensitized nanoporous TiO_2 electrode deposited on a transparent conductive oxide (TCO),

pores filled with iodide (I^-)/triiodide (I_3^-) redox couple electrolyte and platinum electrode, Figure 2.4 [11]. Under photon illumination, excited electrons generated in the dye will be injected to the conduction band of TiO_2 and the injected electron will reach to the TCO electrode by diffusing through the porous TiO_2 network [11]. Electrons will be supplied to the oxidized dye molecule by the liquid electrolyte (Iodide/ triiodide (I^-/I_3^-)) redox couple within the pores in order to reduce the dye to its original state, as shown in Figure 2.4. The oxidized dye accepts electrons from I^- to form I_3^-, and the I_3^- accept electron from platinum to form I^-. Compared to other classes of hybrid solar cells, DSSCs have high power conversion efficiency (PCE). This high PCE value was attributed to the reduced recombination of charge carriers at the interface through a rapid compensation of electrons by the liquid electrolyte [11].

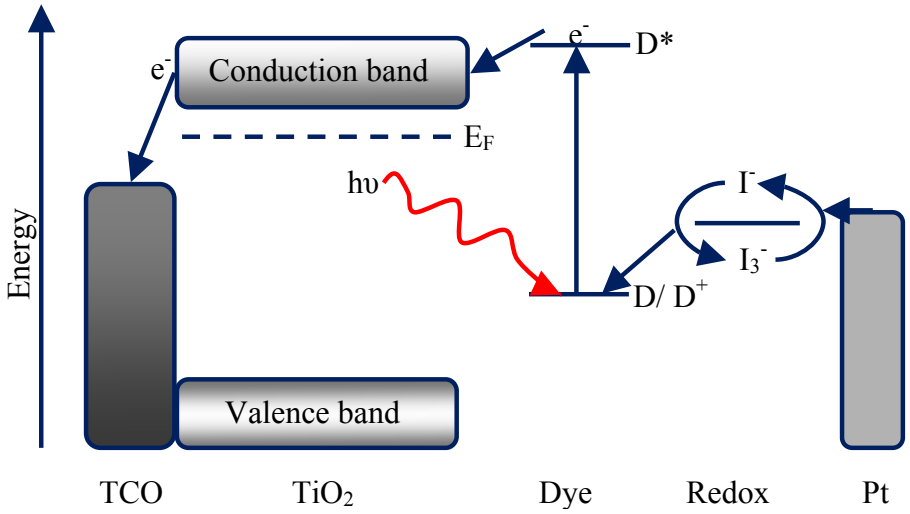

Figure 2.4: Schematic of charge transport and interfacial transfer in DSSCs. D is dye, D* is excited state of the dye, and D^+ is oxidized dye.

The main drawback of DSSC is the presence of a liquid electrolyte, which plays a major role on device instability (sealing problem and facilitate degradation). This limitation was mitigated by replacing either the electrolyte with a p-type semiconductor or by replacing both the dye and electrolyte with conjugated polymers, such as polythiophene derivatives, which can accomplish the task of light absorption, electron injection and hole transport [5, 11]. Nanoporous metal oxide/polymer solar cells are similar to DSSCs except the dye and electrolyte in

DSSCs is replaced by conjugated polymers. Despite the huge surface area provided by the nanoporous TiO_2 layer, the power conversion efficiency of such solar cells remained low as a result of inefficient filling of the pores, high recombination rate at the interface and reduction in hole mobility in infiltrated organic polymers, due to their twisted conformation in the nanosize pores [5].

2.2.2 Inorganic-organic hybrid solar cells

Inorganic-organic hybrid solar cells have been made using several types of semiconducting nanoparticles, such as nanocrystals, nanorods, tetrapods and hyperbranched nanoparticles [13]. It has been found that the power conversion efficiency of solar cells strongly depends on the morphology and size of semiconducting nanoparticles. Solar cells containing nanoparticles with moderate aspect ratio gave the highest power conversion efficiency, on the other hand, those containing nanoparticles with the highest aspect ratio, gave low PCE values [14]. This could be due to nanoparticles with very high aspect ratio tend to aggregate quickly limiting the separation and transport of charge carriers. Selected parameters of semiconducting inorganic nanocrystals used for photovoltaic applications are listed in Table 2.1.

Table 2.1: Selected parameters of semiconducting inorganic nanoparticles used for photovoltaic applications, E_{CB}, E_{VB} , E_g are conduction band energy, valence band energy and bandgap energy respectively [9, 13, 15]

Nanoparticle	E_{CB} (eV)	E_{VB} (eV)	Eg (eV)	Electron mobility (cm^2/ Vs)
ZnO	-4.19	-7.39	3.20	4.00
CdSe	-3.71	-5.81	2.10	600
PbSe	-4.20	-5.02	0.82	2.5
Si-NCs (3-5 nm)	~-4.1	~-5.6	1.5	----

Similarly, various organic polymers have been used for photovoltaic applications, which include: derivatives of vinylene backbones: poly[2-methoxy 5-(2'-ethyl-hexyloxy)-p-phenylenevinylene (MEH-PPV), derivatives of thiophene backbones: poly(3-hexylthiophene) (P3HT), and poly[2,5-bis(3-alkylthiophene-2-yl)thieno[3,2-b]thiophene] (PBTTT), and poly(triarylamine) (PTAA), Figure 2.5. Important parameters of organic polymers used for the construction of hybrid solar cells are listed in Table 2.2.

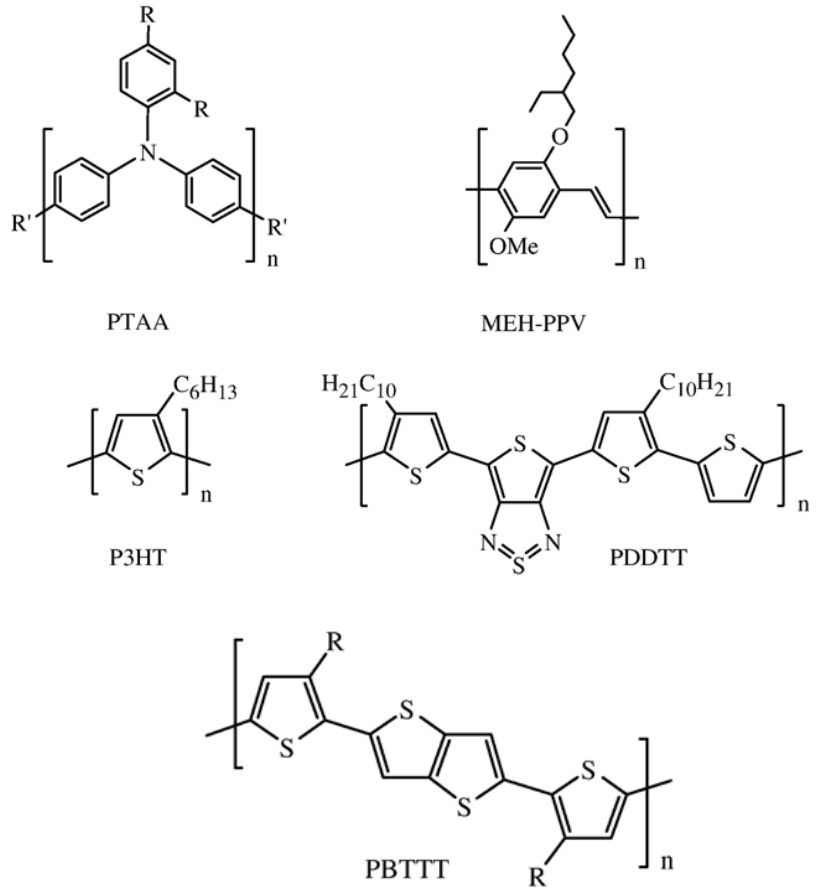

Figure 2.5: Organic semiconductors commonly used to interface with inorganic semiconductors [13].

Table 2.2: Useful parameters of semiconducting polymers used for photovoltaic applications, E_{LUMO} is energy of LUMO, E_{HOMO} is energy of HOMO, and $Eg = E_{LUMO}$-E_{HOMO} is optical bandgap [13]

Polymer	E_{LUMO} (eV)	E_{HOMO} (eV)	E_g (eV)	Hole mobility (cm^2/Vs)
PTAA	-2.00	-5.00	3.00	10^{-4}-10^{-3}
MEH-PPV	-2.90	-5.30	2.40	10^{-4}-10^{-3}
P3HT	-3.00	-5.10	2.10	10^{-4}-10^{-1}
PDDTT	-3.60	-4.70	1.10	-----
PBTTT	-3.60	-5.10	1.50	0.2-0.6

Among all semiconducting organic polymers, P3HT is the most widely used due to its good solubility, processability, environmental stability and high hole mobility [16]. PTAA is less suited for photovoltaic applications due to its wide bandgap. Although the solar energy is distributed from 300 to 1700 nm, Figure

2.6, organic semiconductors absorb only a part of the incident light owing to their larger bandgaps (> 1.9 eV). To overcome this limitation small bandgap conjugated polymers, such as PDDTT and PBTTT having spectral response from 300 to 1450 nm are recently reported [17].

The choice of materials for photoactive layer depends on the extent of exciton dissociation at the donor acceptor interface and their carrier mobility. Furthermore, miscibility between the donor and acceptor materials needs to be considered.

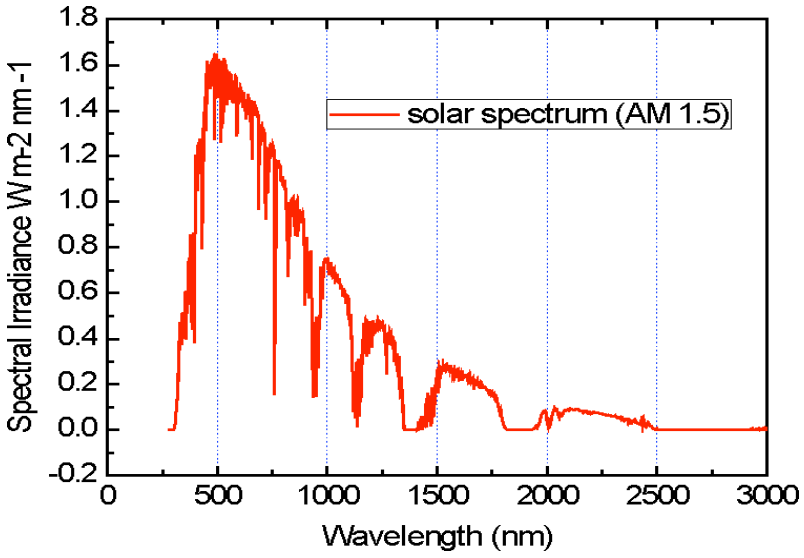

Figure 2.6: Solar irradiation spectrum for AM 1.5 illumination [18].

2.2.2.1 Bilayer photovoltaic cell

Tang *et al*. demonstrated bilayer type heterojunction solar cells for the first time in 1985 [19]. Unger *et al.* recently reported bilayer heterojunction devices using TiO_2 and [tris(dicyno-vinyl-2-thienyl)phenyl]amine layers as acceptor and donor materials, respectively [20]. They also investigated the effect of donor film thickness on the performance of the device. They found a maximum power conversion efficiency of 0.3 % for devices made with a donor thickness of 7.5 nm, Figure 2.7.

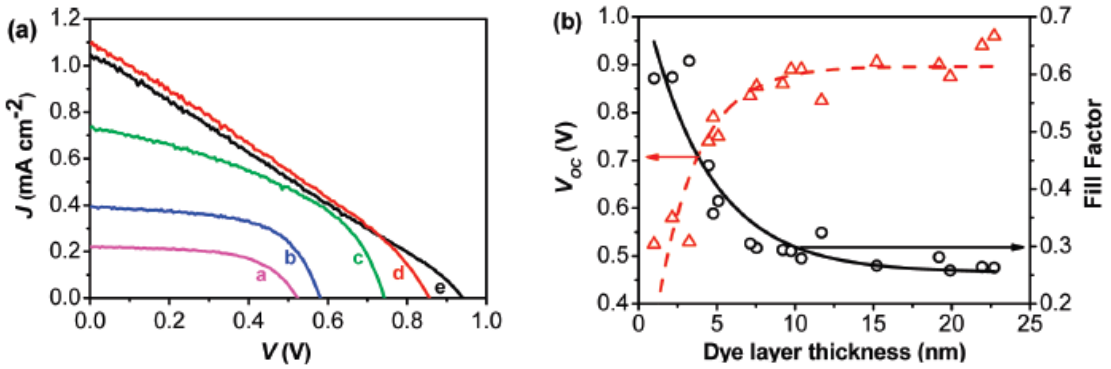

Figure 2.7: (a) Current density *J* vs voltage *V* measurements for bilayer hybrid solar cells with varying donor layer thicknesses: 1 nm (a), 2.2 nm (b), 4.5 nm (c), 7.5 nm (d), and 23 nm (e) on dense TiO_2. (b) Dependency of the open circuit voltage V_{OC} (triangles) and fill factor (circles) on the donor layer thickness [20].

In such devices, the power conversion efficiency depends on charge collection efficiency, which on the other hand is field dependent process. After dissociation of charge carriers at the donor/acceptor junction, holes have to travel through the entire donor material to reach to the back contact. As a result, in the donor material there is a strong competition between charge transport and recombination of electrons and holes.

Gunes *et al.* also fabricated bilayer heterojunction hybrid solar cells using an electron and hole transporting layer of PbS nanocrystals and poly(3-hexylthiophene), respectively [21]. The structure of the device was glass/ITO/nc-PbS/P3HT/Au. The current density versus voltage plots of such devices both in semi logarithmic and linear scale are shown in Figure 2.8.

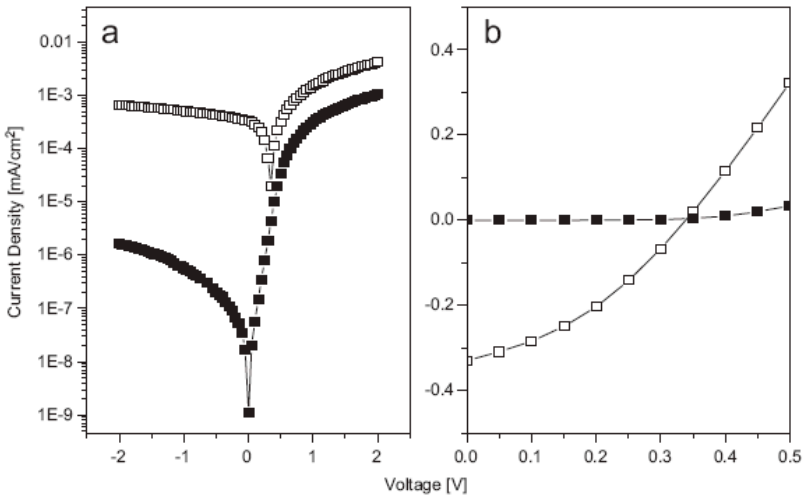

Figure 2.8: I–V characteristics of ITO/PbS/P3HT/Au in (a) semi logarithmic and (b) linear scale [21].

The reported solar cell parameters: short circuit current, open circuit voltage, fill factor and power conversion efficiency were 0.3 mA/cm^2, 350 mV, 35 % and 0.04 %, respectively. The absorption spectra of PbS and P3HT were compared with incident photon to current efficiency (IPCE) of the hybrid solar cell as in Figure 2.9.

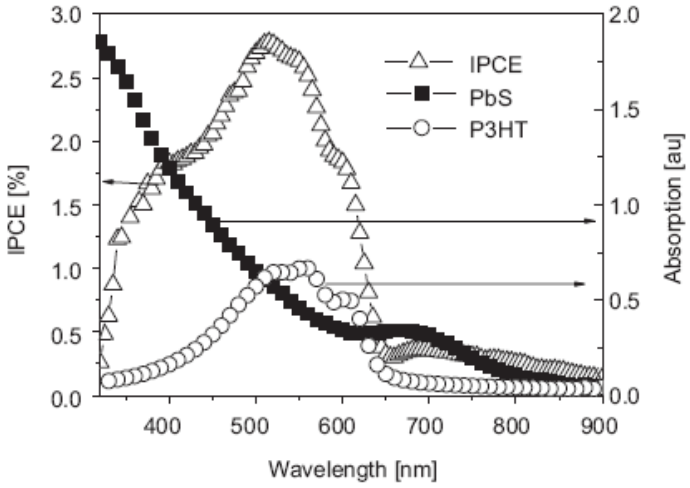

Figure 2.9: Comparison of the IPCE spectra with the absorption spectra of the individual components of P3HT/ PbS hybrid solar cell [21].

Despite the extended absorption spectrum of PbS nanocrystals having absorption edge around 850 nm, the power conversion efficiency of the hybrid solar cell remained too low due to the bilayer nature of the device. The maximum incident photon to current efficiency of this device was reported to be 3 %.

2.2.2.2 Bulk heterojunction photovoltaic cell

Based on bulk heterojunction concept, a number of hybrid solar cells have been reported. Among them the current efficiency record of 2.2 % was held for CdSe/P3HT hybrid solar cells [6]. In this section, BHJ SCs and major factors affecting the performance of hybrid solar cells are reviewed.

Greenham *et al.* demonstrated the first hybrid solar cell based on bulk heterojunction concept in 1996 by incorporating CdSe nanocrystals into MEH-PPV. The reported power conversion efficiency of the hybrid solar cells for AM 1.5 condition at 5 Wm^{-2} was 0.2% [22]. They also described the dependence of solar cell parameters on the size and concentration of semiconductor

nanocrystals. Changing the size of semiconducting nanocrystals alters their bandgap, which in turn changes the absorption spectrum of the device. On the other hand, nanocrystals concentration strongly affects the morphology of the photoactive film and hence affects the power conversion efficiency of the device. They stressed the importance of phase segregation in the photoactive film to enhance the transport of electrons and holes to their respective electrodes without recombination.

Nanocrystals with different structure and morphology have been used to fabricate hybrid solar cells based on bulk heterojunction concept. Figure 2.10 shows transmission electron micrograph (TEM) of CdSe nanocrystals with different aspect ratio [23]. The shape and alignment of the nanocrystals were observed to affect the transport of charge carriers towards the cathode material. While the transport of electrons through a network of smaller nanocrystals is mainly dominated by hoping, nanocrystals with high aspect ratio can penetrate through a larger portion of the device facilitating the transport of electrons towards the cathode.

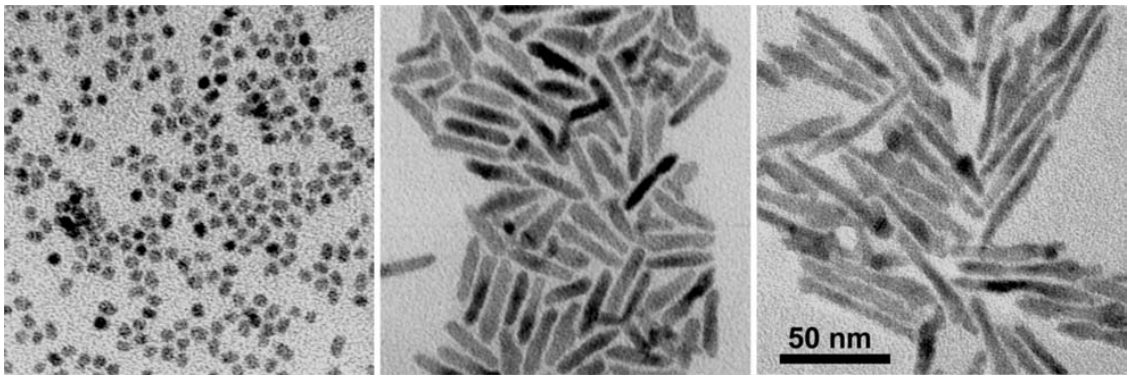

Figure 2.10 TEM images of different shaped CdSe nanocrystals [23].

Kumar *et al.* demonstrated a hybrid solar cell based on CdTe nanorods and MEH-PPV [24]. The reported power conversion efficiency of the hybrid solar cell was 0.05 %. The presence of insufficient percolation network, nanoparticle agglomeration and large phase separation were mentioned as the main reasons for the very low power conversion efficiency. Compared to CdSe/MEH-PPV hybrid solar cells, higher power conversion efficiency value was expected for CdTe/MEH-PPV hybrid solar cells. The absorption edge of CdTe nanocrystals is

located in the near infrared region, hence they absorb significant part of the solar spectrum as a result enhanced device performance was expected.

Other nanocrystals such as PbS (Eg=0.37 eV) and PbSe (Eg=0.26 eV) were attractive materials for solar cell applications because of their ability to absorb over a wide range of spectrum, up to near infrared radiation of the sunlight [25]. However, their low bandgap was found to reduce the open circuit voltage significantly, which eventually affect the power conversion efficiency. Hence, although the use of low bandgap nanocrystals enhances photocurrent generation, the decrease in open circuit voltage has a strong effect on the power conversion efficiency [25].

Hybrid solar cells based on oxide nanocrystals of ZnO have also been reported [26]. Compared to nanocrystals based on Pb and Cd, oxides nanocrystals are environmentally friendly and are relatively inexpensive. Ji *et al.* demonstrated a hybrid solar cell containing an active layer made by blending nanocrystalline ZnO with regioregular P3HT [26]. They used both ZnO nanodots and nanorods to study how the morphology of the nanocrystals affects the performance of hybrid solar cells.

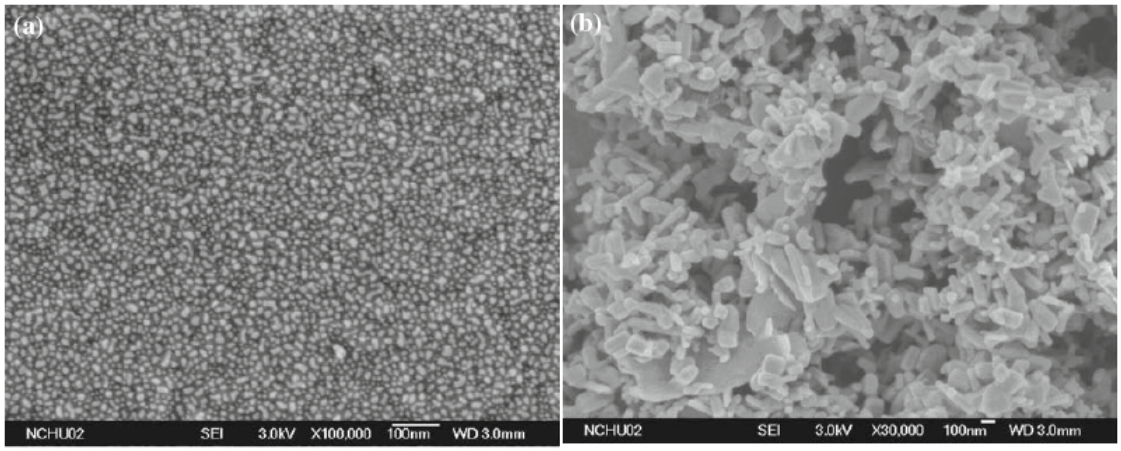

Figure 2.11: FESEM images of a) ZnO nanodots and b) ZnO nanorods [26].

The structure of the device was, glass/ITO/PEDOT:PSS/70 wt.% nc-ZnO-P3HT/Al with an active area of 0.35 cm^2. The current density versus voltage characteristics of the solar cell, which was carried out under a simulated AM 1.5 illumination with highest power density of 100 mW/cm^2, is shown in Figure 2.12. In Figure 2.12, hybrid solar cells made using ZnO nanodots have got a short

circuit current density and an open circuit voltage of 0.4 mA/cm^2 and 0.22 V, respectively, with a power conversion efficiency of 0.036 %. The short circuit current density and open circuit voltage of devices made with ZnO nanorods were 0.16 mA/cm^2 and 0.32 V respectively, and their power conversion efficiency was 0.020 %. The results showed that hybrid solar cells made from ZnO nanodots are 1.8 times more efficient than those made from ZnO nanorods. Although the use of nanorods can enhance the transport of electrons towards the cathode, the high surface area of ZnO nanodots, which is around ten times higher than ZnO nanorods, was found to play a dominant role for effective dissociation of excitons and transfer of charge from P3HT to ZnO nanodots.

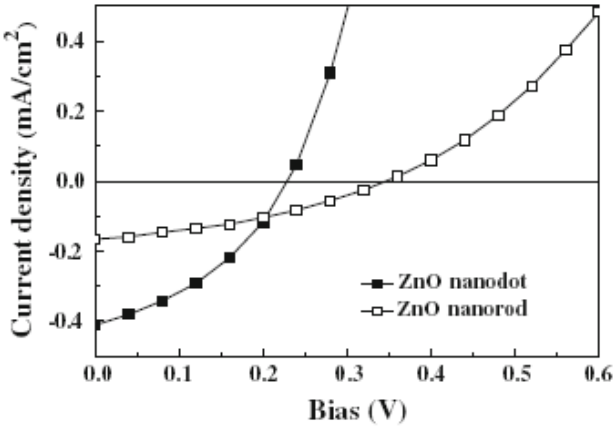

Figure 2.12: Current density–voltage (J–V) characteristic of nc-ZnO/P3HT solar cells under a simulated AM 1.5 illumination with light density of 100 mW/cm^2 [26].

2.3 Potential of Si-NCs and P3HT for solar cell application

The choice of acceptor materials for photovoltaic applications depends on the match between the energy levels of acceptor and donor materials, Figure 2.13. In addition to this the absorption band of nanocrystals needs to match better with the maximum irradiance of the solar spectrum, Figure 2.6, where the optimum direct bandgap was estimated to be 1.5 eV [27]. Studies show that the bandgap of Si-NCs having size greater than 5 nm is comparable to the bulk bandgap, 1.12 eV, while Si-NCs having size less than 5 nm exhibit wider bandgap as a result of quantum confinement effect [28]. The HOMO and LUMO of Si-NCs having size 4 nm was estimated to be -5.6 and -4.1

respectively relative to the vacuum energy level [6]. As the highest occupied molecular orbital (HOMO) and lowest unoccupied molecular orbital (LUMO) of P3HT are laying at -5.1 and -2.9 eV relative to the vacuum level, it can be used with Si-NCs for efficient dissociation of excitons at the interface [9]. Aluminium and ITO electrodes can be used for effective extraction of electrons and holes respectively due to their suitable work function values, Figure 2. 13. Liu *et al.* recently investigated the effect of varying Si-NC/P3HT weight ratio for different Si-NC sizes on the power conversion efficiency of Si-NC/P3HT hybrid solar cells [9]. They achieved a maximum power conversion efficiency of 1.15 %, 0.5 % and 0.18 % for solar cells made from 35 wt.% Si-NC/P3HT (nanocrystal size 3-5 nm), 35 wt.% Si-NC/P3HT (nanocrystal size 5-9 nm), and 65 wt.% Si-NC/P3HT (nanocrystal size 10-20 nm) respectively [9]. They also observed that both the open circuit voltage and short circuit current increased with decreasing Si-NC size. Although only few large size Si-NCs are needed to make interconnected pathways for electrons, which can enhance to the charge collection efficiency, higher current density value has been obtained for smaller size Si-NCs. This implies that electron transport through the nanoparticles was not a limiting factor.

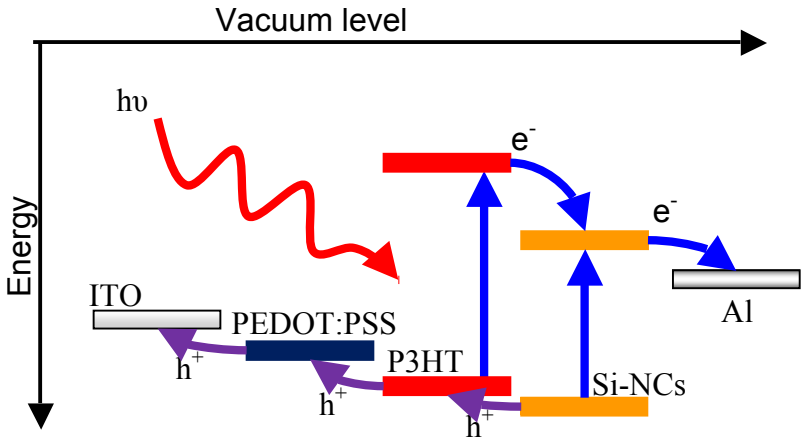

Figure 2.13: Energy band diagram for Si-NC/P3HT hybrid solar cells.

2.3.1 Silicon nanocrystals

Compared to other inorganic semiconductors, silicon nanocrystals are promising candidate for fabrication of hybrid photovoltaic devices because of their low production cost with a very high yield, non-toxicity, solution processability, high abundance and compatibility with conjugated polymers [14]. Moreover, the optical bandgap of silicon nanocrystals can be increased by decreasing their size due to quantum confinement effect as a result their absorption spectrum can be tuned [9], Figure 2.14.

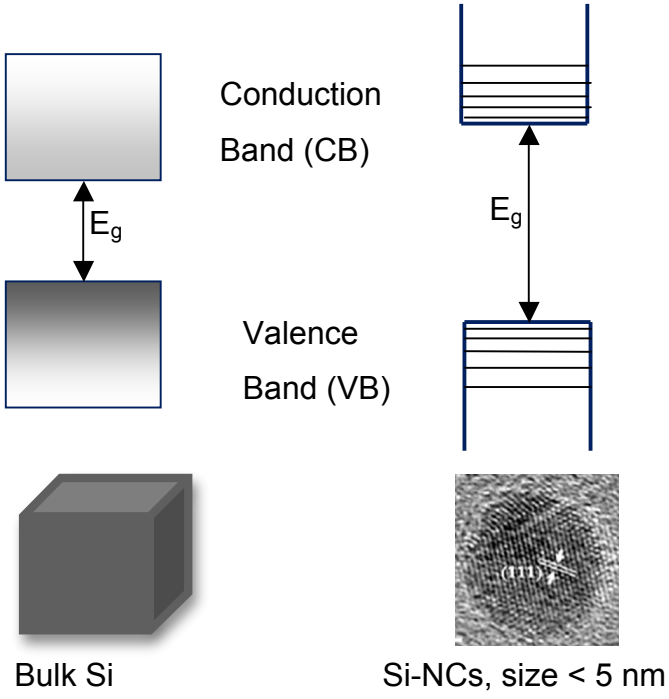

Figure 2.14: Variation of bandgap of silicon with size

Various methods have been proposed for the synthesis of silicon nanocrystals including, thermal evaporation of Si or SiO, laser induced and plasma enhanced chemical vapour deposition (PECVD) [29]. Plasma based synthesis of silicon nanocrystals has attracted much attention in present years because of reduced risk of contamination and possibility of mass production with minimized particle agglomeration [9, 29]. Plasmas are grouped into nonthermal and thermal. The major difference between them is, while the later is in thermal equilibrium, the former is not in thermal equilibrium as the ions' or radicals' temperature is different from the temperature of electrons. Nonthermal plasma synthesis of

silicon nanocrystals from silane is becoming attractive as it can be done at reduced temperature.

In a microwave nonthermal plasma synthesis, a high microwave (MW) power has been used to generate a very high electric field. This very high electric field will accelerate electrons to high energy under low pressure to induce nonthermal plasma. Due to their higher mass the energy of ions is much less than electrons. As a result of this energy difference, electrons are considered as hot (T=50,000 K) and ions or neutrals are considered as cold (T= 500 K). The precursor gas will dissociate as a result of collision with hot electrons.

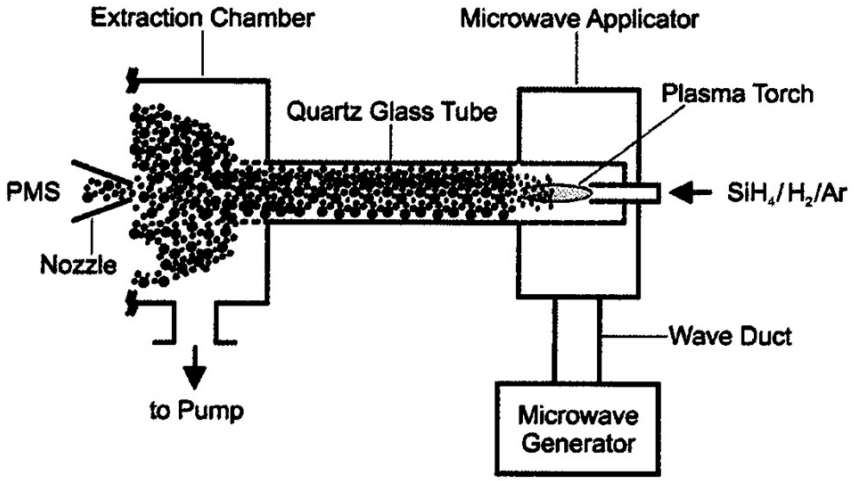

Figure 2.15: **Schematic drawing of the low pressure microwave reactor for the preparation of silicon nanoparticles [29].**

A typical setup for the preparation of Si-NCs is shown in Figure 2.15. The main parts of the reactor consist of a mixture of reaction and dilution gases inlet, microwave system with microwave generator, wave duct and microwave applicator, quartz glass tube, particle extraction chamber consisting of particle mass spectrometer (PMS) and pumping system. A microwave generator is used to create an electric field that can accelerate electrons at high energy to a gas under low pressure to excite and ionize the silane gas atoms. Hot electrons in the plasma are effective in dissociating silane precursor gas to form silane radicals. These radicals cluster chemically to form nanoparticles. In the quartz tube reactor the microwave energy is coupled into the inlet gases (SiH_4, H_2, Ar) to produce a flam-like plasma torch. The generated particles are separated from the exhaust gas through a molecular beam system and collected on a surface

[29]. A study showed that unsaturated Si_nH_m clusters have high electron affinity [30]. As a result plasma electrons will be attached to the clusters and hence the clusters become negatively charged and electrostatically suspended in the plasma.

The mean diameter of Si-NCs depends on the initial silane concentration, gas pressure and microwave power. Knipping *et al.* found that the mean diameter of Si-NCs increased with increase in silane concentration and decreased with increase in microwave power [29].

2.3.2 Poly (3-hexylthiophene) (P3HT)

P3HT is the most widely used conjugated polymer for solar cell application. With the exception of its low solubility, which resulted due to the strong π-π interaction, polythiophene has excellent thermal stability (42% weight loss at 900 ^{0}C), and high electrical conductivity (3.4 x 10^{-4} to 1.0 x 10^{-1} S/cm when doped with iodine). To increase the solubility of polythiophene in organic solvents, a flexible alkyl chain is attached at the polymer backbone. It was demonstrated that polythiophenes having an alkyl group greater than butyl can be melt, or solution processed into films [31]. It was also found that, upon oxidation poly(3-alkylthiophene) can have an electrical conductivity as high as, 40 ± 5 S/cm [31]. As a result of the asymmetry of 3-alkylthiophene molecules a number of arrangements between adjacent thiophene rings is reported, Figure 2.16.

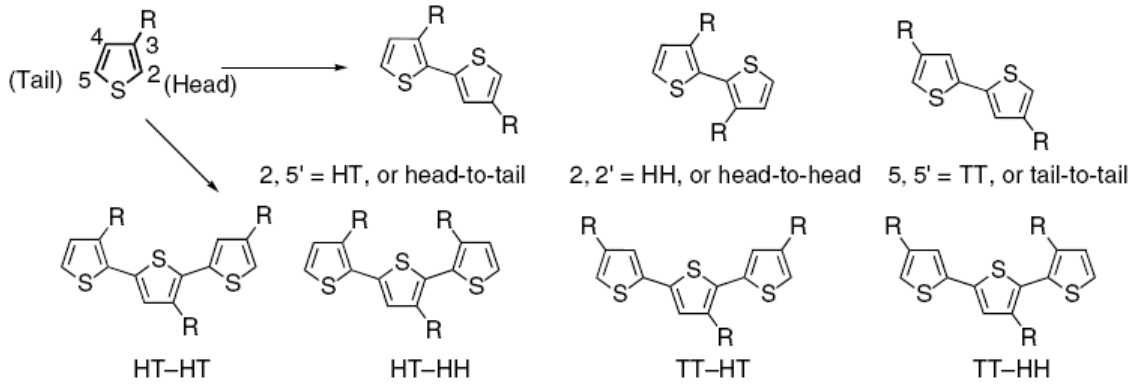

Figure 2.16: Classical synthetic methods lead to a number of regiochemical isomers [31].

Polymers made from random coupling between 3-alkylthiophene molecules are denoted as regiorandom or non-HT. On the other hand polymers made of

controlled HT couplings are termed as regioregular or HT. Regioregular poly(3-alkylthiophene) (P3AT) has high electrical conductivity due to the planar arrangement of polymer backbone, which give rise to three dimensional self-assembly, and hence enhanced inter-chain and intra-chain conductivity pathways. Regiorandom P3AT with HH couplings loss their conjugation as a result of increased torsion angle between the thiophene rings. The increase in torsion angle between thiophene rings widens the bandgap, which in turn degrades the electrical and optical properties of the polymer.

For photovoltaic applications, shorter alkyl chains, hexyl and octyl are preferred as they have higher mobilities (0.03 – 0.05 cm^2/Vs) due to the longer π-π overlap distance between polythiophene backbones. The electrical conductivity of 80% regioregular poly(3-hexylthiophene) samples was reported to be 6 S/cm [31].

In recent years, P3HT attracted lots of attention as a donor material in organic solar cells mainly due to its absorption edge around 650 nm, and its high hole mobility. Organic solar cells with best power conversion efficiencies approaching 5 % were made from blends of P3HT and fullerene derivatives [32].

3. Experiments

3.1 Materials and chemicals

Si-NCs with mean diameter of about 46.8 nm were obtained from *Institut für Verbrennung und Gasdynamik,* University of Duisburg-Essen, Germany. As produced and oxidized Si-NCs having a mean size of 3-5 nm were obtained from University of Minnesota, United States of America. The NCs were grown in a low pressure microwave plasma reactor by microwave induced decomposition of silane [33]. The mean diameter of Si-NCs was adjusted to 46.8 nm by adjusting the concentration and pressure of process gases and the microwave power. ITO coated glass substrates, having a dimension of 100 mm x100 mm x1.1 mm, were purchased from Optical Filters Ltd, UK. Poly(3,4ethylenedioxy-thiophene):poly(styrenesulfonate) (PEDOT:PSS) (1.3 wt.% dispersion in water) and regioregular Poly(3-hexylthiophene-2,5-diyl) were purchased from Sigma Aldrich. Cholorobenzene and cleaning agents, acetone and ethanol were also purchased from Sigma Aldrich.

3.2 Etching of silicon nanocrystals

As grown silicon nanocrystals are terminated with Si-H bonds, but form a native oxide layer upon exposure to air [34]. The formation of this insulating layer hinders the migration of electrons towards the cathode. To remove this insulating oxide layer, Si-NCs were etched in hydrofluoric acid (5 vol.% in water) for one minute by placing them on vacuum system using 0.1 µm polyvinylidene fluoride (PVDF) membrane filters (Millipore). The HF-etched silicon nanocrystals were rinsed with ethanol 2-3 times to remove the excess acid, afterwards filtered and dried under vacuum. Ultrasonic treatment was used to release the nanocrystals from the filter and disperse them in chlorobenzene.

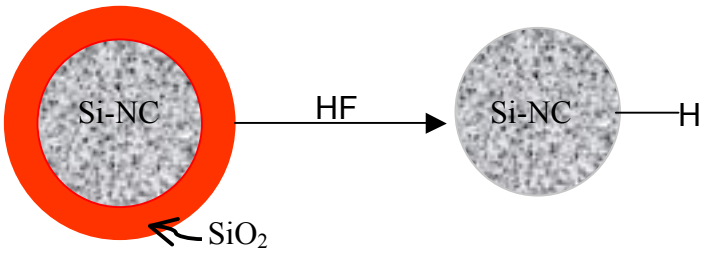

Figure 3.1: HF etching of low-pressure plasma synthesized silicon nanocrystals.

3.3 Equipments

An ultrasonic bath (Bandelin Sonorex, RK255) having a power of 300 W and frequency of 40 KHz has been used for sonication. A spincoater (speedline Technologies model P6708) was used to deposit PEDOT:PSS, P3HT and Si-NC/P3HT films onto ITO coated glass substrates. This spin coater was obtained from APT GmbH, Germany. Dektak profilometer (Veeco 150) was used to measure the thickness of P3HT, PEDOT:PSS, and Si-NC/P3HT films. The vacuum oven used for annealing has been obtained from Fornos Electricos, Lda, Portugal.

3.4 Characterization techniques

In this section the working principles and experimental conditions of characterization techniques used to investigate hybrid solar cells are described.

3.4.1 UV- visible spectroscopy

A UV-3600 UV-VIS-NIR spectrophotometer was used to measure the optical transmittance of the different films making up the hybrid solar cell. This system is equipped with three detectors: a photomultiplier tube (PMT) for the UV-visible region (162 – 1000 nm), an InGaAs detector (700 – 1800 nm), and a PbS detector (1600 – 3300 nm) for the near infrared region. The radiation sources were tungsten filament for the region between 300 to 2500 nm and deuterium arc lamp for ultraviolet region, 190 to 400 nm. The instrument measures the light intensity passing through the sample, I, and compares it with the incident light, I_o. The ratio between the intensities of the outgoing light to the incident light is called transmittance (T). The absorbance, A, is related to the transmittance through,

$$A = -\log T$$

3.4.2 Fourier transform infrared spectroscopy

Fourier transform infrared (FTIR) spectroscopy is certainly an important tool to characterize the surface chemistry of nanoparticles in general and silicon nanoparticles in particular [34]. The FTIR technique is based on the interference between two infrared radiation beams. A beam splitter made of semi-reflecting film is used to divide the incident beam into two parts. The choice of beam

splitter material depends on the region to be examined. For mid-infrared regions (4000 to 400 cm^{-1}) germanium coated potassium bromide (KBr) substrates are used. The reflected beam travels to a fixed mirror and returns back; the transmitted beam travels to the moving mirror and returns back to the beam splitter. An optical path difference between the two beams reaching to the beam splitter is produced as a result of the moving mirror before they recombine and produce an interference pattern. The intensity of transmitted infrared radiation versus change of path length between the two beams yields an interferogram. A mathematical method of Fourier transformation is used to convert distance domains into frequency and vice versa. Absorption peaks in FTIR spectra occur when the frequency of vibration of the bonds between atoms match with the frequency of infrared radiation. These absorption peaks are unique and hence indicate the molecular structure of samples.

The FTIR spectra were acquired in reflection mode at room temperature using an evacuated Bruker IFS 66v spectrometer. Potassium bromide (KBr) was used as beam splitter. The detector used was deuterium tryglycine sulfate (DTGS). 200 scans have been accumulated in each measurement.

3.4.3 Current-voltage measurements

3.4.3.1 Electrical characterization of hybrid solar cells

To analyse the I-V characteristics of solar cells it is useful to create a model as shown in Figure 3.2 [35].

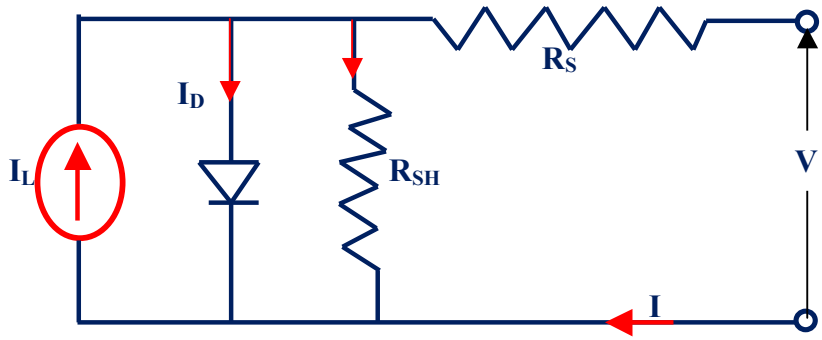

Figure 3.2: Equivalent circuit model for solar cells

From Figure 3.2, the current produced by the solar cell is given by [35]

$$I = I_L - I_D - I_{SH} \tag{7}$$

where I_L is the photogenerated current, I_D is the current flowing through the diode, and I_{SH} is the current flowing through the shunt resistor.

The voltage across the diode, which is the same as the voltage across the resistor R_{SH} can be written as,

$$V_i = V + IR_S \tag{8}$$

where R_s is the series resistance which accounts for Ohmic losses due to the bulk resistance of the photoactive layer and metallic contacts, V is the voltage across the output terminal, and I is the output current.

The current through the diode is given by Shockley equation as,

$$I_D = I_0\left[\exp\left(\frac{qV_i}{nkT}\right) - 1\right] \tag{9}$$

where I_0 is saturation current, n is the ideality factor, which provides information on the quality of junction, q is the charge, k is Boltzmann's constant and T is temperature.

The shunt resistance (R_{SH}), which accounts for the leakage of current across the heterojunction, is related to I_{SH} by,

$$I_{sh} = \frac{V_i}{R_{sh}} \tag{10}$$

Substituting Equations 8 – 10 in 7, the current-voltage characteristics of hybrid solar cells under illumination is given by,

$$I = I_L - I_o\left(\exp\left[\frac{q(V + IR_s)}{nkT}\right] - 1\right) + \frac{V + IR_s}{R_{SH}} \tag{11}$$

Solar cell parameters, such as, I_0, R_s and R_{SH} depend on the size of the solar cell, to exclude this effect the I-V characteristic equation of solar cells is usually written in terms of current density, J, as,

$$I = J_L - J_o\left(\exp\left[\frac{q(V + JAR_s)}{nkT}\right] - 1\right) + \frac{V + JAR_s}{AR_{SH}} \tag{12}$$

where J_0 is reverse saturation current density, J_L photo-generated current density, and A is active area of the device.

The J-V curve of solar cells under illumination has the shape shown in Figure 3.3. From Figure 3.3, performance parameters of the solar cell can be determined. The short circuit current (I_{SH}) is related to the short circuit condition

when the impedance is low and it is determined at zero applied voltage. For ideal solar cell, the short circuit current is equal to the photo-generated current. The open circuit voltage (V_{OC}) is determined when there is no current passing through the solar cell. The power produced by the solar cell is given by,

$$P = IV \Rightarrow P_{Max.} = I_{Max.}V_{Max.} \tag{13}$$

This power is zero at I_{SC} and V_{OC} and has a maximum in between. The power conversion efficiency, η, is the ratio of the output electrical power (P_{out}) to the solar power input (P_{in}) into the solar cell under standard test conditions, at temperature of 25 °C, and an irradiance of 1000 W/m^2 with an air mass 1.5 spectrum.

$$\eta = \frac{P_{out}}{P_{in}} \Rightarrow \eta_{Max.} = \frac{P_{Max.}}{P_{inc.}} \tag{14}$$

The Fill factor (*FF*) is given by

$$FF = \frac{I_{\max.}V_{\max.}}{I_{SC}V_{OC}} \tag{15}$$

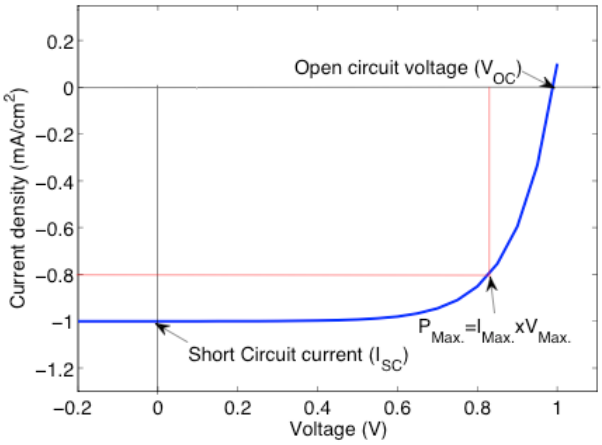

Figure 3.3: Shape of I-V curve for solar cells

3.4.3.2 Equipment of the electrical measurements

Current versus voltage characteristics for the hybrid solar cells and photoactive films were measured using a Keitley 228 A voltage current source and Keithley 2000 multimeters. Air Mass 1.5 Global (AM 1.5) solar simulator with irradiance intensity of 1000 W/m^2 has been used to measure the performance of the hybrid solar cells. A 50 W halogen lamp powered with Delta Elektronika ES 030-10 power supply has been used as a light source.

3.4.4 Scanning electron microscopy

Scanning electron microscope (SEM) has been used to study the morphology of Si-NC/P3HT photoactive films. To acquire SEM images, the photoactive films were scanned with a high-energy electron beam. The secondary electron produced as a result of the interaction of the electron beam with atoms near to the surface was used to reveal the details of the photoactive film at high magnification. A Hitachi SU-70 analytical scanning electron microscope (Japan) was used to record images of Si-NC/P3HT (1:1 and 2:1 wt.%) photoactive films and cross section of Si-NC/P3HT hybrid solar cells. The samples were sputtered with a thin layer of carbon to minimize the effect of charging.

3.4.5 Electron paramagnetic resonance (EPR)

EPR has been used to estimate the concentration of defects in oxidized and HF-etched Si-NCs. This technique is based on the interaction between unpaired electrons and a magnetic field. In the presence of an external magnetic field, either electron's magnetic moment aligns parallel to the magnetic field (lower energy) or aligns antiparallel to the magnetic field (higher energy). Absorption of a microwave radiation (9 – 10 GHz) results in promotion of unpaired electrons from lower to higher energy state. The absorption of microwave frequency gives EPR spectra, where the integrated intensity of the peak is proportional to the concentration of unpaired electrons and hence defects in the nanocrystals.

EPR spectra were taken using Bruker ESP 300E EPR X-band spectrometer. 15.1 and 9.1 mg of unetched and HF-etched Si-NCs respectively were inserted separately into small plastic tubes, which were sealed at one of their ends with epoxy glue. After compressing the nanocrystals, the other ends of tubes were sealed with a polytetrafluoroethylene (PTFE) tape. The sealed tube containing Si-NCs was placed at the end of a quartz tube and then kept in the middle of the EPR resonator to acquire the spectra.

4. Experimental data and discussion

4.1 Silicon nanocrystals

A scanning electron microscope was used to investigate the shape and size of Si-NCs used for the fabrication of hybrid solar cells. FTIR measurements were also done to study the effect of HF etching on the surface structure of Si-NCs.

4.1.1 SEM image of silicon nanocrystals

For SEM analysis, suspensions of HF-etched Si-NCs in chlorobenzene were drop-casted onto ITO coated glass substrates. The resulting Si-NC films were dried in a vacuum oven at 120 ^{o}C for 20 minutes. Although the mean diameter of Si-NCs is 46.8 nm, from Figure 4.1 it can be clearly seen that there are few Si-NCs having size greater than 100 nm. These large Si-NCs settle fast and hence could facilitate Si-NC aggregation.

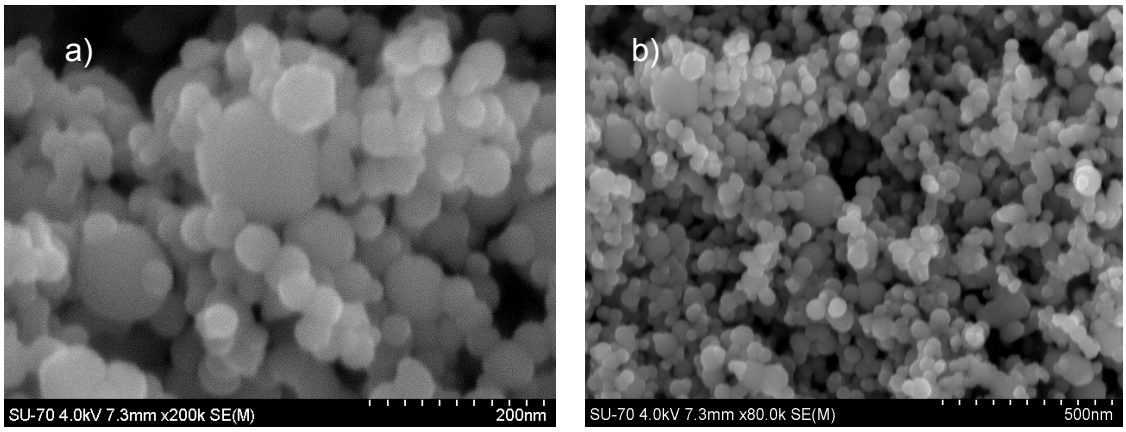

Figure 4.1: SEM image of HF-etched Si-NCs; a) and b) are taken at different magnification.

4.1.2 FTIR spectra of silicon nanocrystals

To acquire the FTIR spectra, suspension of HF-etched Si-NCs in chlorobenzene was drop-casted onto a gold-coated polyimide Kapton substrate. As shown in Figure 4.2, for HF etched Si-NCs the peak around 1111 cm^{-1} in the absorbance spectrum corresponds to Si-O-Si stretching vibration, which occurred as a result of the exposure of silicon nanocrystals film to air for 5 hours. The peak around 2084 cm^{-1} can be decomposed into three major peaks that are related to Si-H stretching vibration of silicon hydrides, Si-Si–H_3, Si_2-Si-H_2 and Si_3-Si-H [34]. The appearance

of these peaks is expected as the silicon nanocrystals surface is terminated with Si-H bonds after HF etching. The peak at 2250 cm^{-1} corresponds to vibrational stretching of Si-H in the presence of oxygen back bonding (O_3-Si-H). On the other hand the peak around 2197 cm^{-1} is attributed to vibrational stretching of Si-H in either O_2-Si-H_2 or O_2-Si-Si-H [34]. In Figure 4.2, FTIR spectrum of HF-etched Si-NCs is compared with the spectrum of unetched Si-NCs [36]. As shown in the figure, the relative intensity of Si-O-Si band reduced drastically after HF etching. Moreover, the intensity of Si-H_x band is higher than the intensity of O_3-Si-H band for HF-etched Si-NCs. This shows that HF etching is effective to remove SiO_2 oxide layer.

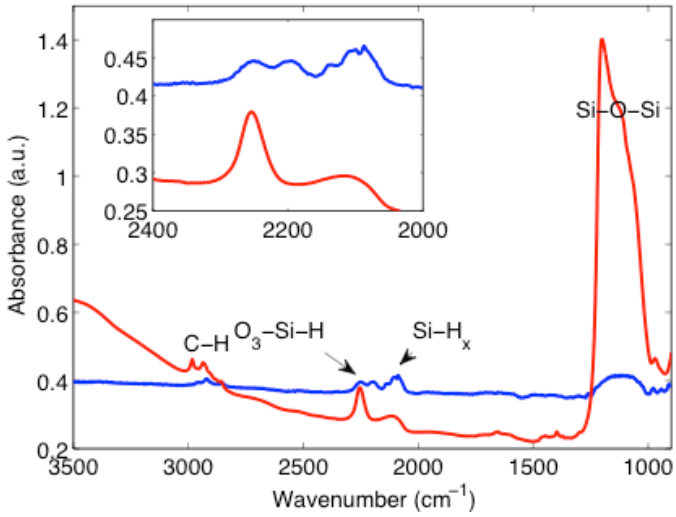

Figure 4.2: FTIR absorption spectra of non-thermal plasma prepared oxidized silicon nanocrystals (red line) and HF-etched silicon nanocrystals (blue line). The films were deposited from their suspension in chlorobenzene onto gold-coated Kapton polyimide substrate. The inset shows magnification of absorbance spectra from 2400 to 2000 cm^{-1}.

4.2 Poly(3,4 ethylene-dioxythiophene): poly(styrenesulfonate) (PEDOT:PSS)

4.2.1 UV-visible absorption spectrum of PEDOT:PSS

In hybrid solar cells, a thin layer of PEDOT:PSS was spin-coated onto ITO coated glass substrates to improve the transport of holes, as its work function is higher than ITO and lower than P3HT. However, as the illumination is done through the ITO side, the PEDOT:PSS layer should be transparent to AM 1.5 illumination. To confirm this, the transmittance of a 100 nm thick PEDOT:PSS

film spin-coated onto ITO coated glass substrate was measured as a function of wavelength (Figure 4.3). The thickness of PEDOT:PSS layer used in most hybrid solar cells reported so far is between 50-100 nm. About 100 nm thick PEDOT:PSS film was found after spin coating 20 μL of PEDOT:PSS (as received 1.3 wt.% suspension in water) onto ITO coated glass substrate at 3000 rpm for 30 seconds and annealing at 150 ^{o}C for 20 minutes. The thickness of the film was estimated using Veeco Dektak 150 surface profiler. The film was scratched with a needle to determine its height from the ITO layer. It can be seen that, the transmittance of PEDOT:PSS from 300 to 1000 nm is very high, as a result it is transparent to AM 1.5 radiation.

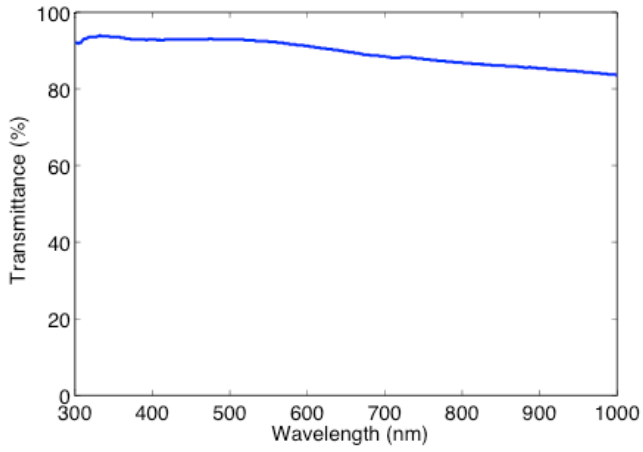

Figure 4.3: UV-visible spectrum of PEDOT:PSS film deposited on ITO coated glass substrate. The UV-visible spectrum of ITO coated glass substrate was taken as a reference.

4.3 Poly(3-hexylthiophene) (P3HT)

UV-visible and FTIR measurements were done to confirm the optical absorption and chemical structure of P3HT films, respectively. Photo- and dark conductivity measurements were also done to investigate the stability of P3HT film in air.

4.3.1 UV-visible absorption spectrum of P3HT film

For UV-visible measurement, a solution of P3HT in chlorobenzene (10 mg/mL) was spin coated onto ITO coated glass substrate at 3000 rpm for 30 seconds and dried under vacuum at 150 ^{o}C for 20 minutes. The thickness of the resulting film was 65 nm. The thickness of the film was measured using Veeco Dektak 150 surface profiler by scratching the film with a needle and measuring its

height from the ITO layer. Figure 4.4, shows the UV–visible absorption spectrum of a 65 nm thick P3HT film. The UV-visible spectrum of the P3HT film showed two peaks at 524 nm and 551 nm and one shoulder at 596 nm. These three bands can be attributed to the π–π* transition in crystalline π-stacking structure of P3HT [37].

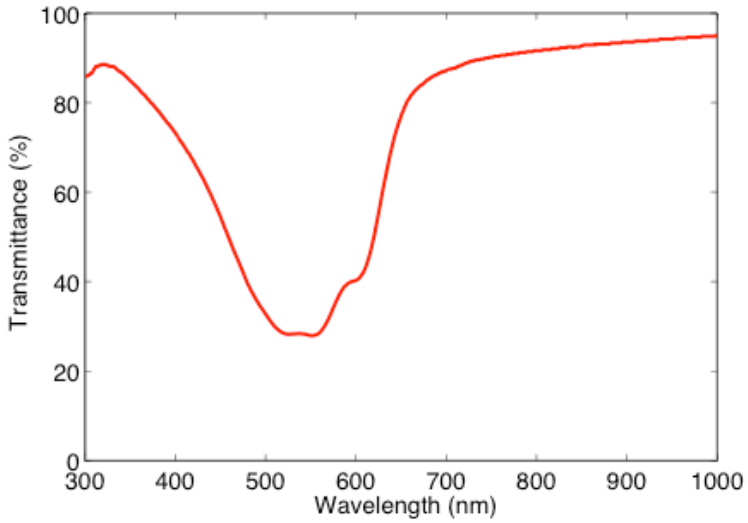

Figure 4.4: UV-visible spectrum of P3HT film deposited onto ITO coated glass substrate. The UV-visible spectrum of ITO coated glass substrate was taken as reference.

4.3.2 FTIR spectrum of P3HT film

To acquire FTIR spectrum a solution of P3HT in chlorobenzene (10 mg/mL) was drop-casted onto a gold-coated polyimide Kapton substrate. Figure 4.5 shows FTIR spectra of pristine P3HT film in the range from 4000 to 500 cm^{-1}. The vibrational band at 818 cm^{-1} corresponds to out of plane vibration of =C-H which is characteristic of regioregular P3HT, where individual P3HT molecules are arranged in head to tail (2, 5-) configuration [16]. The vibration bands at 2800 – 3100 cm^{-1} appeared due to C-H_x bonds in P3HT. The ratio of asymmetric and symmetric C=C stretching absorption peaks in P3HT at 1509 and 1455 cm^{-1} was found to be related to the conjugation length [16]. The ratio of these two peaks for our P3HT film was 0.48, which is less than the value (0.53) reported for pristine P3HT used in [15]. This indicated that the P3HT we used for the fabrication of the solar cells should be less conductive.

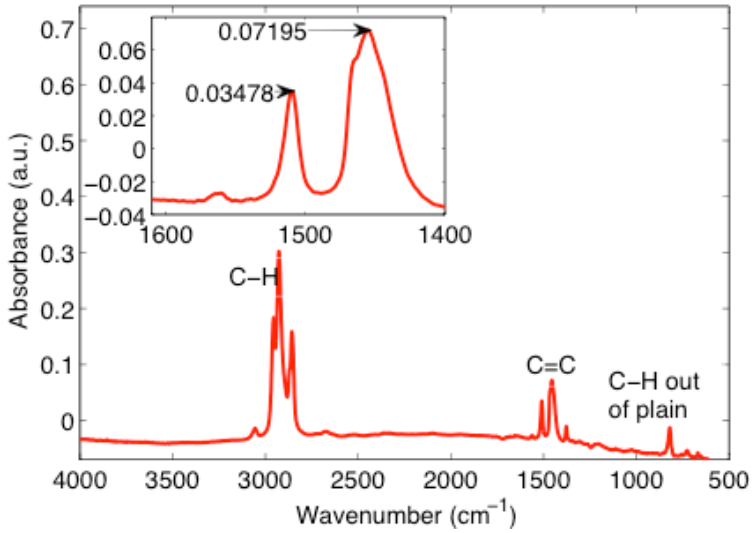

Figure 4.5: FTIR spectrum of pristine P3HT, the inset shows asymmetric, 1509 cm^{-1} and symmetric, 1455 cm^{-1} peak.

4.3.3 Conductivity of P3HT film

The photoelectric property of P3HT films was studied in a parallel photoconductivity measurement where, 5 µL solution of P3HT in chlorobenzene (10 mg/mL) was drop-casted onto interdigitated gold electrodes deposited on a polyimide substrate. The film was annealed at 120 ^{0}C under vacuum for 20 minutes. The resulting thickness of the film was 1.77 µm. The current-voltage measurements were done in air. The thickness of the film was determined using a profilometer.

Figure 4.6 shows that the current through the P3HT film increase with air exposure time for both measurements done under AM 1.5 illumination and in dark, which could be due to crystallization of P3HT with time.

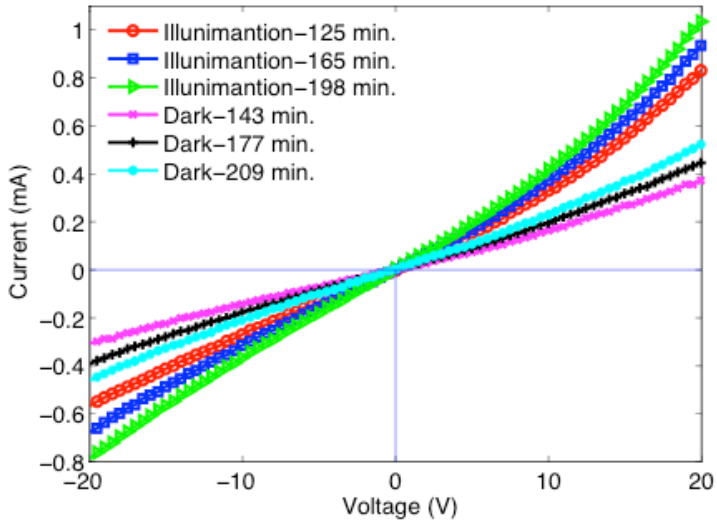

Figure 4.6: I-V characteristics of P3HT film drop-casted onto interdigitated gold electrodes; done under Am 1.5 illumination and in dark. The I-V measurement was done after exposing the film in air for 125, 165 and 198 minutes.

For a film having thickness *t*, width *w*, and length *L*, the resistance *R* is given by

$$R = \rho \frac{L}{A} \tag{4.1}$$

where *ρ* is the resistivity and $A=wt$ is the cross sectional area of the film.

From, Equation 4.1, the resistivity, *ρ* can be rewritten as,

$$\rho = \frac{RA}{L} = \frac{Rwt}{L} \Rightarrow \sigma = \frac{1}{\rho} = \frac{L}{Rwt} = \frac{IL}{Vwt} \tag{4.2}$$

where $R=V/I$, and *σ* is conductivity.

For our film deposited onto interdigitated electrodes, *L* is the distance between the electrodes, 10 µm, *w* is the length of the electrodes, 2 mm, and *t* is the thickness of the film, 1.77 µm. From the I-V curve, the conductivity of P3HT film was calculated by taking the current at 20 V.

Since the number of electrodes n, is equal to 112, the average conductivity of P3HT film can be written as,

$$\sigma = \frac{IL}{nVwt} \tag{4.3}$$

Figure 4.7 a) shows the change in photo- and dark- conductivity of a P3HT film with air exposure time. Although the film was exposed to air for a long time, we did not observe degradation of conductivity rather an increase in conductivity has been observed. In Figure 4.7 b) the change in photo to dark conductivity

ratio with air exposure time is shown. From the figure it can be clearly seen that the photo to dark conductivity ratio decreased from 2.4 to 1.06 upon exposing the film in air for 360 h. The results show that although both the photo and dark conductivities of P3HT did not show degradation upon air exposure, the P3HT film losses its photosensitivity with air exposure time.

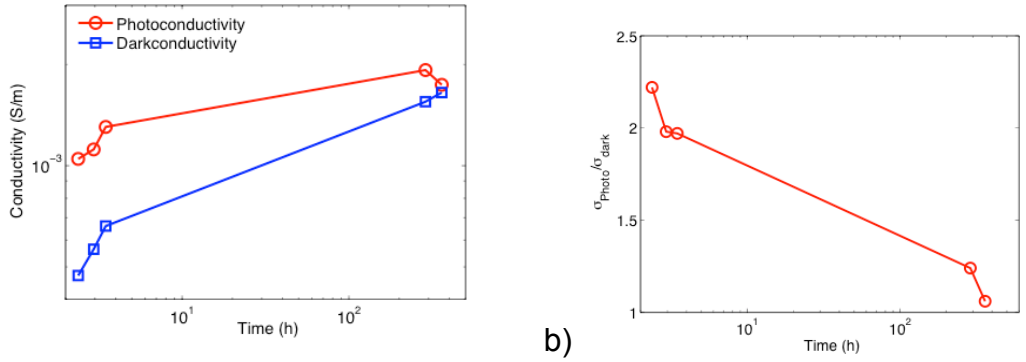

Figure 4.7: a) change in photo and dark conductivity of P3HT film with air exposure time, b) change of photo to dark conductivity ration of P3HT film with air exposure time. The P3HT film was made by drop-casting 5 µL of P3HT solution in chlorobenzene onto Kapton substrate coated with interdigitated gold electrodes. The resulting film was annealed at 120 ^{0}C for 20 minutes in vacuum. The photoconductivity was measured under AM1.5 illumination an in dark.

4.4 Si-NC/P3HT photoactive layers

SEM was used to analyse the morphology of photoactive films made from HF-etched Si-NC/P3HT (at 1:1 and 2:1 wt.%). HF-etched Si-NC/P3HT blends were made by dissolving 10 mg of Si-NC and 10 mg of P3HT (1:1 wt.%) in 1 mL of cholorobenzene and 20 mg of Si-NC and 10 mg of P3HT (2:1 wt.%) in 1 mL of cholorobenzene, respectively. It has been studied that the morphology of the photoactive film has a strong effect on the power conversion efficiency of the solar cells [38]. Moreover, it is believed that the degradation of the device is mainly due to degradation of the photoactive film. To investigate this we have studied the change of conductivity of the photoactive layer with air exposure time.

4.4.1 SEM imaging

In Figure 4.8, (a) and (b) correspond to SEM images of HF-etched Si-NC/P3HT film at 1:1 wt.%, (c) and (d) correspond to SEM images of HF-etched Si-NC/P3HT film at 2:1 wt.%. For SEM analysis HF-etched Si-NC/P3HT films were made by drop casting 10 µL of the blend suspension in chlorobenzene onto 0.5x0.5 cm ITO coated glass substrates. All films were annealed at 120 ^{o}C for 20 minutes in vacuum.

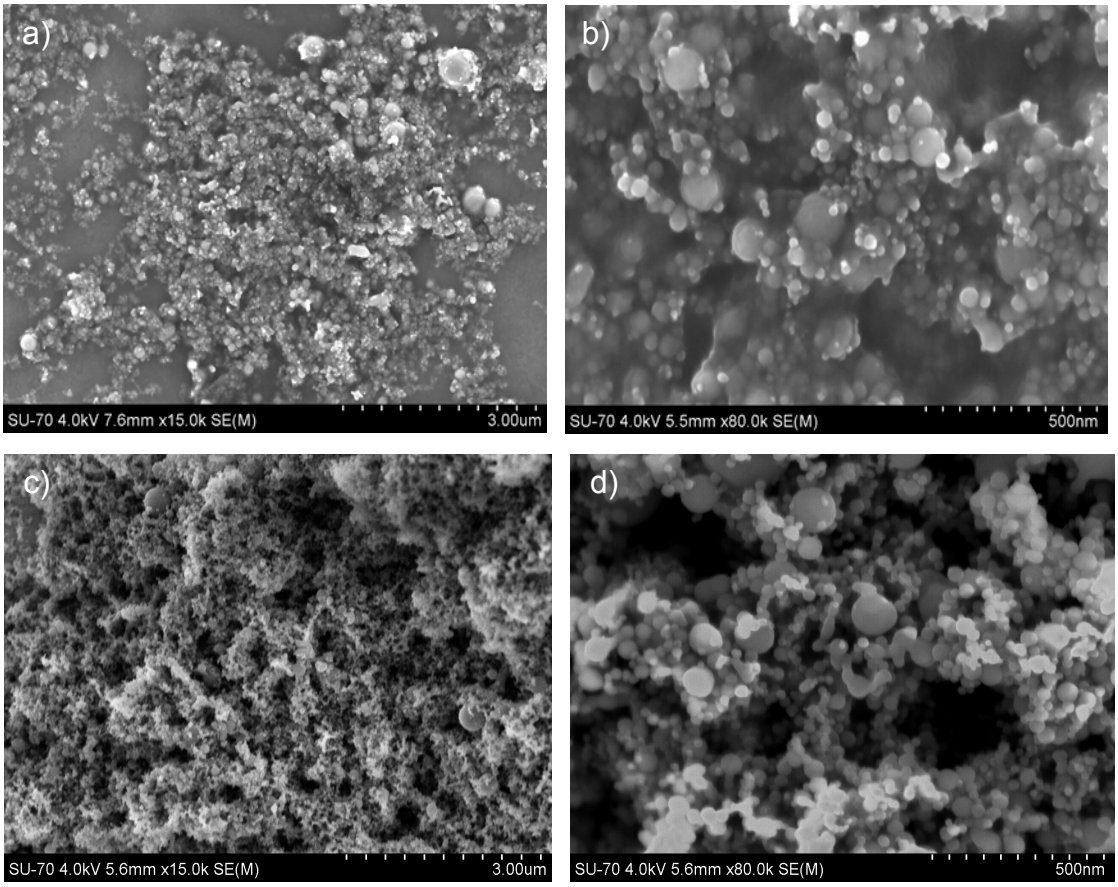

Figure 4.8: SEM image of HF-etched Si-NC/P3HT blend drop-casted onto ITO coated glass substrate at 1:1 Si-NC:P3HT wt.%: a) at 3 µm, b) at 500 nm and at 2:1 Si-NC:P3HT wt.%: c) at 3 µm, d) at 500 nm.

The morphology of photoactive films made from 1:1 (Si-NC/P3HT) wt.% did not show sufficient interpenetrated network throughout the photoactive layer, Figure 4.8 a). On the other hand films made from 2:1 (Si-NC/P3HT) wt.% show the formation of interpenetrated network throughout the photoactive layer, Figure 4.8 (c and d). This shows that the 2:1 wt.% concentration should be the better one for the solar cell devices.

4.4.2 UV-visible absorption spectra of HF-etched Si-NCs/P3HT (1:1 wt.%) film

To acquire UV-visible spectra, suspension of Si-NC/P3HT (1:1 wt.%) in chlorobenzene was spin coated onto ITO coated glass substrate at 1500 rpm for 30 seconds and annealed at 150 ^{o}C for 20 minutes in vacuum. The resulting thickness of the film was 210 nm. The thickness of the film was measured using a profilometer. The spectrum of Si-NC/P3HT (1:1 wt.%) film is shown in Figure 4.9. When compared with the spectrum of a pristine P3HT film, the spectrum shows a lower transmittance below 500 nm, which is probably due to light absorption in Si-NCs.

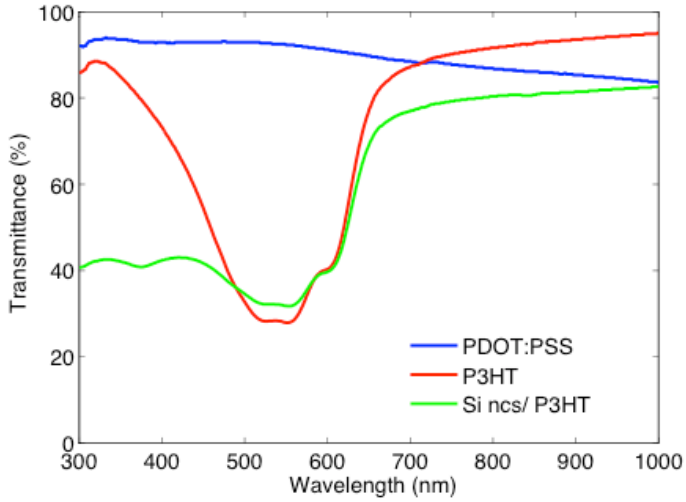

Figure 4.9: UV-visible spectra of PEDOT:PSS (about 100 nm thick), P3HT (about 65 nm thick), and P3HT/ Si-NCs (about 210 nm thick) films spin-coated onto ITO coated glass substrate. The UV-visible spectrum of ITO coated glass substrate was taken as reference.

4.4.3 Conductivity of Si-NC/P3HT films made of HF-etched and unetched-Si-NCs

The photo and dark conductivities of HF-etched Si-NC/P3HT and unetched Si-NC/P3HT films were measured to study the effect of air on the conductivity of the films. The films were made by drop-casting 5 µL of Si-NCs (HF-etched or unetched)/P3HT suspension in chlorobenzene (20 mg of Si-NCs + 10 mg of P3HT/mL of chlorobenzene) onto a polyimide substrate covered with interdigitated gold electrodes. The interdigitated electrodes contain 112 fingers with a length of 2 mm separated by 10 µm. All films were dried at 120 ^{o}C for 20

minutes in vacuum. The resulting thickness of the films was about 2.33 µm. The thickness of the films was determined using Dektak profilometer by measuring the height of the film from the polyimide substrate.

The change of I-V curves of HF-etched Si-NCs/P3HT film with air exposure time is shown in Figures 4.10. As shown in the figure, both photo- and dark- current of Si-NC/P3HT film increase with air exposure time. This could be due to the improved ordering of P3HT chains with time, similar to what we proposed for the P3HT films.

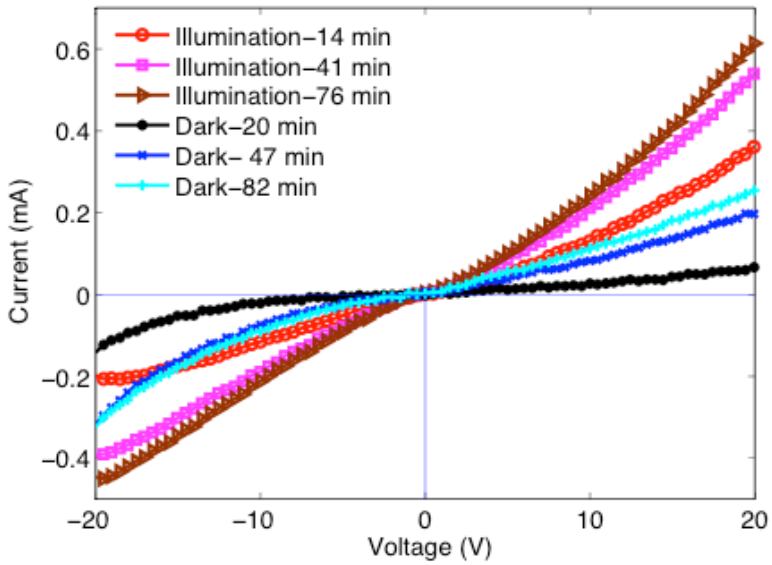

Figure 4.10: I-V characteristics of HF-etched Si-NC/P3HT film drop-casted onto interdigitated gold electrodes; done under AM 1.5 illumination and in dark after exposing the films in air for 14, 41 and 76 minutes.

The conductivity of both HF-etched and unetched Si-NC/P3HT films were calculated from the I-V curve using Equation 4.3 by taking the current at 20 V. The change in both photo- and dark- conductivity of pristine P3HT, HF-etched Si-NC/P3HT and unetched Si-NC/P3HT films with air exposure time are compared in Figure 4.11. The conductivity of pristine P3HT film was higher than the conductivity of HF-etched Si-NC/P3HT and unetched Si-NC/P3HT films by nearly one and two orders of magnitude, respectively. This could be due to the poor quality of the film and due to the presence of silicon nanocrystal aggregates, Figure 4.8, which can distract the ordering of P3HT chains and increase the resistance of the film.

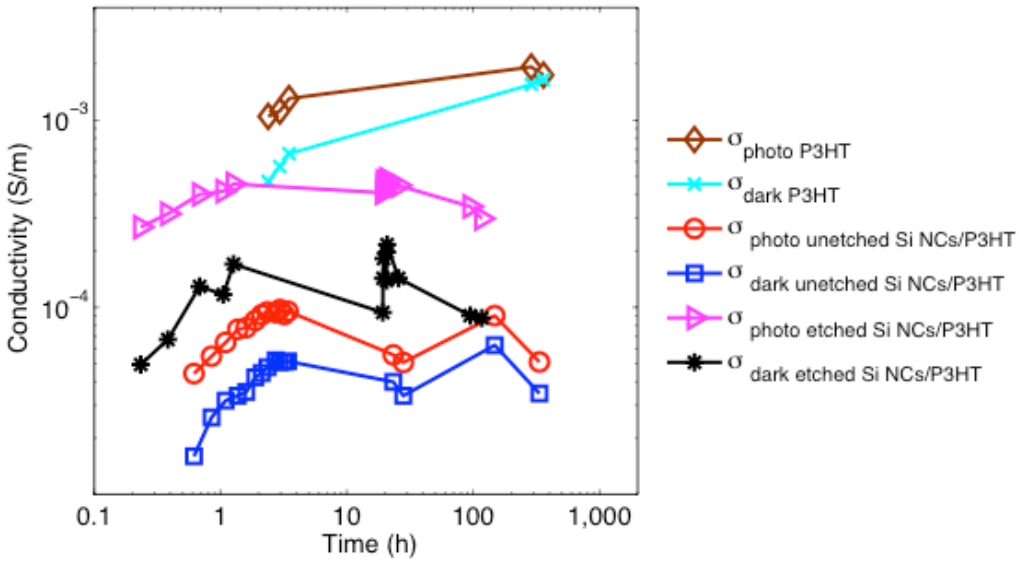

Figure 4.11: Comparison of change in photo and dark conductivity of HF-etched Si-NC/P3HT (2:1 wt. %), unetched Si-NC/P3HT (2:1 wt.%) and pristine P3HT films with time. The measurements were done in air.

As shown in Figure 4.11, both the photo- and dark- conductivities of HF-etched Si-NC/P3HT film were higher than photo- and dark conductivity of unetched-Si-NCs/P3HT film. The conductivity of both films increased with time for the first few hours and then became nearly stable over a long time. As shown in Figure 4.12, the photo- to dark-conductivity ratio of HF-etched Si-NC/P3HT film is higher than the photo- to dark- conductivity ratio of unetched Si-NC/P3HT film. This indicates that HF etching of Si-NCs improved charge dissociation at Si-NC/P3HT interface, and/or enhanced the transport of charge carriers through Si-NCs network.

Although the conductivity of the films increases with air exposure time, the photo to dark conductivity ratio was found to decrease with air exposure time, Figure 4.12. This indicates that the photoactive films loss their photosensitivity upon air exposure. This could be related to degradation of the devices in air.

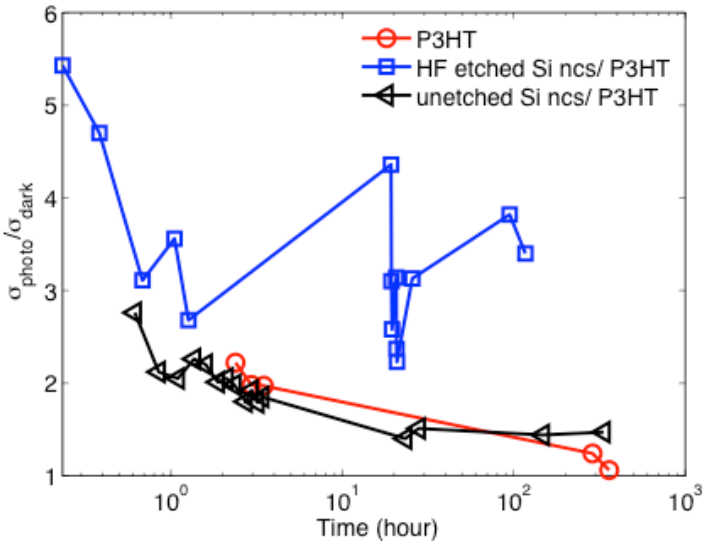

Figure 4.12: Change of photo- to dark- conductivity ratios of P3HT, HF-etched Si-NC/P3HT and unetched Si-NC/P3HT films with air exposure time. Conductivity measurements were done under AM 1.5 illumination and in dark in air.

4.5 Si-NC/P3HT hybrid solar cells

In this section the fabrication of Si-NC/P3HT hybrid solar cells is presented. Then results for I-V characterization of hybrid solar cells made from 1:1 and 2:1 wt.% (Si-NC:P3HT) are presented and discussed.

4.5.1 Fabrication of Si-NC/P3HT hybrid solar cells

To fabricate the Si-NC/P3HT hybrid solar cells, indium tin oxide (ITO)-coated glass substrates were cut into 1 cm by 1 cm substrates and cleaned with acetone and ethanol. 20 µL of PEDOT:PSS (1.3 wt.% suspension in water) was spin-coated onto ITO-coated glass substrates at 3000 rpm for 30 seconds. The resulting PEDOT:PSS film was then annealed at 150 ^{0}C for 20 minutes under vacuum. The thickness of the film was about 100 nm. A hybrid blend was made by dissolving 10 mg of HF-etched Si-NCs and 10 mg of P3HT (1:1 wt.%) in 1 mL of chlorobenzene. Hybrid blends were also made by dissolving 20 mg of HF-etched/unetched Si-NC and 10 mg of P3HT (2:1 wt.%) in 1 mL of cholorobenzene. All blends were sonicated for 10 minutes to minimize agglomeration of Si-NCs. For all solar cells, the photoactive layer was made by spin coating 20 µL of the Si-NC/P3HT blend onto the PEDOT:PSS layer at 1500 rpm for 30 seconds. The resulting Si-NC/P3HT films were annealed at 150 ^{0}C

for 20 minutes in vacuum. The top aluminium electrode was deposited on the photoactive layer by thermal evaporation of aluminium under vacuum lower than 10^{-5} mbar. The solar cells were then scribed with a needle to form smaller cells having an active area of 0.25 cm^2. HF-etched Si-NC/P3HT hybrid solar cells were also made under nitrogen atmosphere following similar procedures except spin coating and annealing of the PEDOT:PSS and Si-NC/P3HT layers were done in nitrogen atmosphere.

4.5.2 Current–voltage characterization of hybrid solar cells made from Si-NC/P3HT with 1:1 wt.%

Figure 4.13 shows the I-V characteristics of Si-NC/P3HT hybrid solar cells made from a blend prepared at 1:1 HF-etched Si-NC/P3HT wt.%. As shown in the figure, rectification behaviour has been observed both in dark and under illumination. As expected for these structures the current under illumination is higher than the current in dark. The rectification under illumination at ±2 V (*I(+2 V)/I(-2 V)*) was 4.75. Although rectification behaviour has been seen, no detectable photovoltaic effect has been observed. The power conversion efficiency of hybrid solar cells strongly depends on exciton generation, exciton dissociation into free charge carriers and transport of charge carriers to their respective electrodes. All these steps depend on the morphology of the photoactive film. As the device fabrication and characterization was done at ambient conditions, degradation of the device due to oxygen and humidity could be expected. To see the effect of air exposure time on the I-V characteristic, we monitored this for different times, Figure 4.14. It can be clearly seen that after 288 h, the I-V characteristics in dark and under AM 1.5 illumination are nearly identical. The main effect is that the photo-effect disappears.

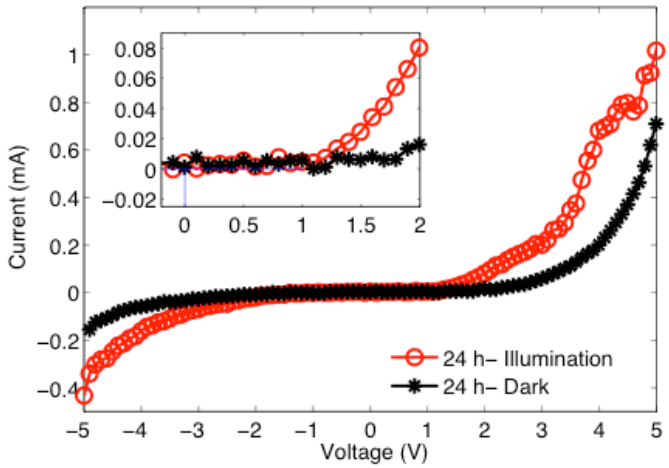

Figure 4.13: I-V curves for hybrid solar cells made from a freshly prepared Si-NC/P3HT blend at 1:1 Si-NCs: P3HT wt. %. I-V measurement was done 24 h after fabrication of the device in dark and under AM 1.5 illumination. The device was kept in a desiccator before I-V measurement.

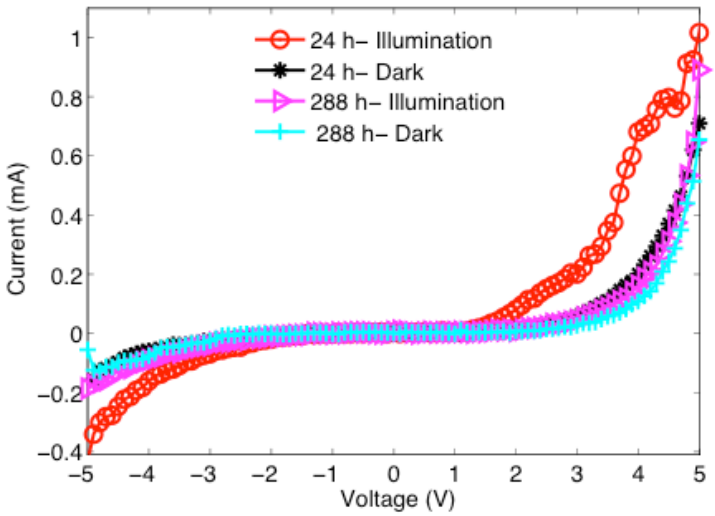

Figure 4.14: Comparison of I-V curves for the same device measured at 24 h and 288 h after device fabrication

SEM cross sectional image of a hybrid solar cell made from 1:1 wt.%(Si-NC/P3HT) is shown in Figure 4.15. From the figure, the thicknesses of Si-NC/P3HT, Al contact and ITO layers were estimated to be 130 nm, 1.16 µm and 142 nm, respectively.

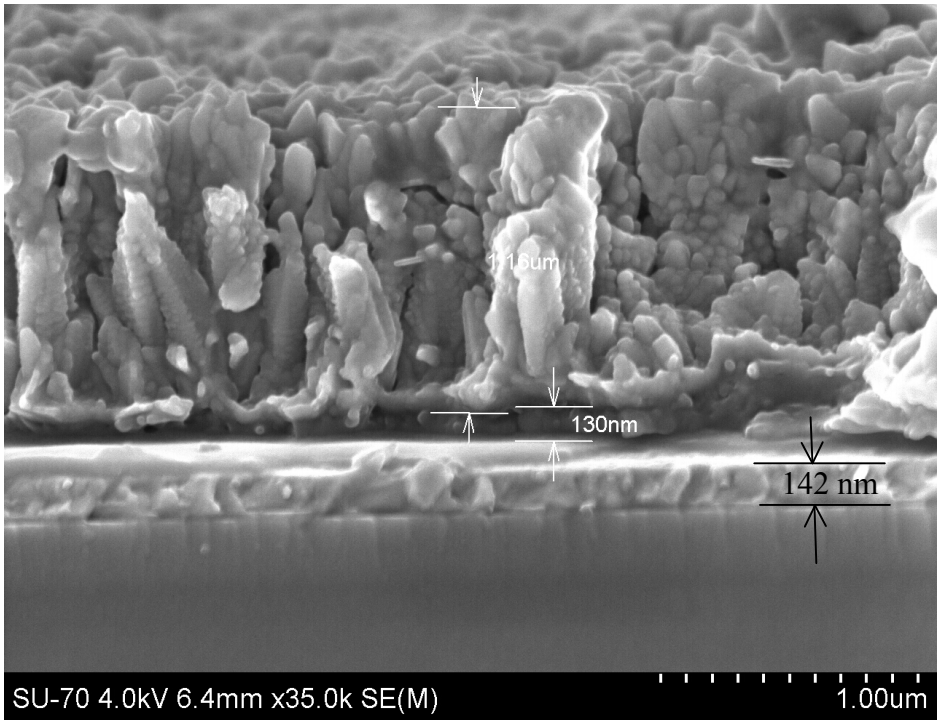

Figure 4.15: SEM cross section of Si-NC/P3HT hybrid solar cell made from 1:1 wt.% (Si-NC:P3HT).

4.5.3 Current–voltage characterization of hybrid solar cells made from Si-NC/P3HT with 2:1 wt.%

The I-V characteristics of the hybrid solar cells made at 2:1 (Si-NCs: P3HT) wt.% are shown in Figure 4.16. Measurements were done 1 h after production of the cells. During this time they were kept in air. The rectification under illumination at ±2 V (*I(+2 V/I(-2 V))*) was 4.01 and 3.1 for plots shown in Figure 4.16 (a) and (b), respectively. In the present situation a very small photovoltaic effect was observed. The hybrid solar cell performance parameters are given in Table 4.1.

a)

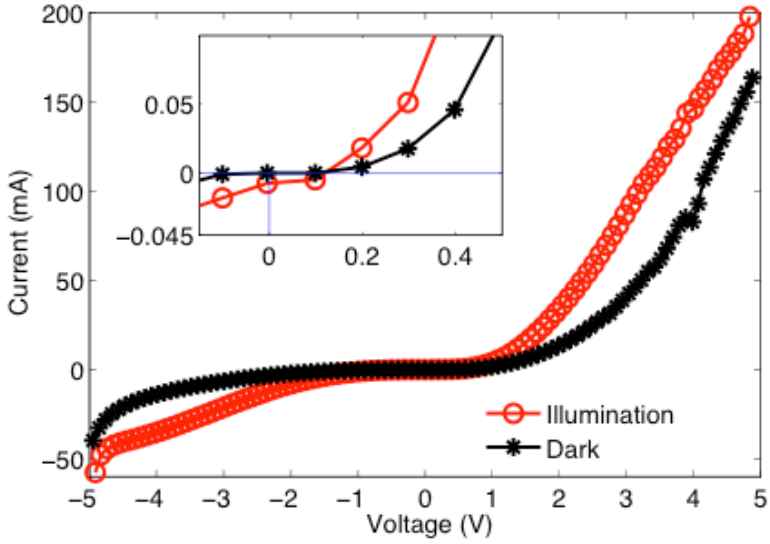

b)

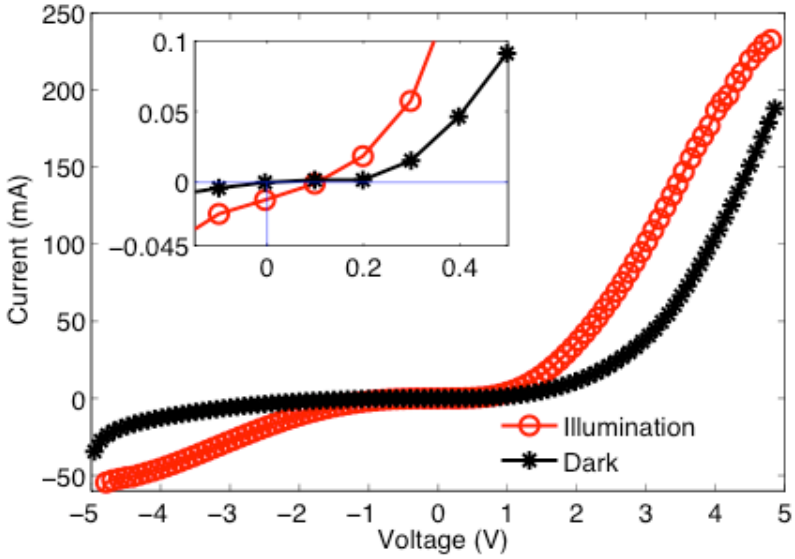

Figure 4.16: I-V curves for hybrid solar cells made from freshly made Si-NC/P3HT blend at 2:1 (Si-NCs: P3HT) wt. % a) and b) corresponds to I-V curves for two devices made on the same substrate. In both cases the I-V behaviour around zero is shown in the inset plots. I-V measurements were done in air under A.M 1.5 illumination and in dark.

Both the short circuit current and open circuit voltage we obtained are much lower than values obtained for the Si-NC/P3HT hybrid solar cells reported previously [9].

Figure 4.17 shows the comparison of I-V characteristics of HF-etched Si-NC/P3HT hybrid solar cells done after exposing the devices in air for 1 h and 26 h. The corresponding solar cell parameters are compared in table 4.1. From the

table it can be seen that the performance of the solar cells degraded after exposing the devices to air for nearly 26 hours.

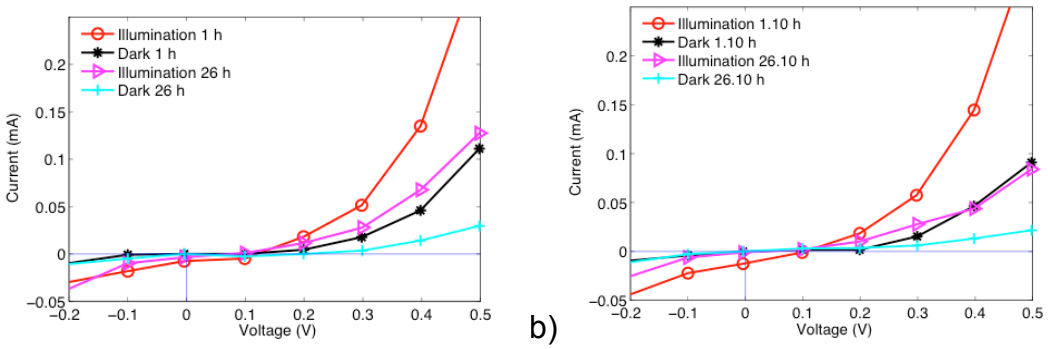

Figure 4.17: Comparison of I-V curves for the same device measured at 1 h and 26.10 h after device fabrication. The devices were kept in air after Al evaporation. The I-V measurements were done under AM 1.5 illumination and in dark.

Table 4.1: 2:1 wt.% HF-etched Si-NC/P3HT solar cell performance parameters

Device	Air exposure time (h)	Short circuit current (μA)	Open circuit voltage (mV)	Solar cell efficiency (%)
Shown in Figure 4.17 a	1	-7.41	121.1	3.5×10^{-5}
Shown in Figure 4.17 a	26	-3.55	76.61	1.1×10^{-5}
Shown in Figure 4.17 b	1.1	-12.12	105.7	5.1×10^{-5}
Shown in Figure 4.17 b	26.1	-1.19	55.65	2.6×10^{-6}

Furthermore, to investigate the degradation of HF-etched Si-NC/P3HT hybrid solar cells upon air exposure, the current at ±4.5 V was monitored with time. As shown in Figure 4.18, the current at ±4.5 V decreased quickly in the first four hours. This quick decrease could be due to air degradation of the device.

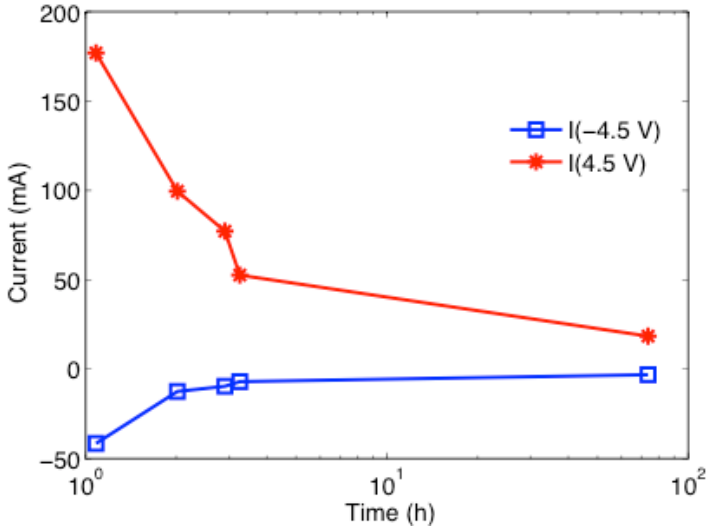

Figure 4.18: Air degradation of HF-etched Si-NC/P3HT hybrid solar cell. The current at ±4.5 V has been monitored to study the degradation of the solar cell with time.

Figure 4.19 shows cross sectional image of a hybrid solar cells made from 2:1 wt.% (Si-NC/P3HT). From the figure, the thicknesses of the photoactive layer and aluminium contact were estimated to be 410 nm and 1.2 µm, respectively.

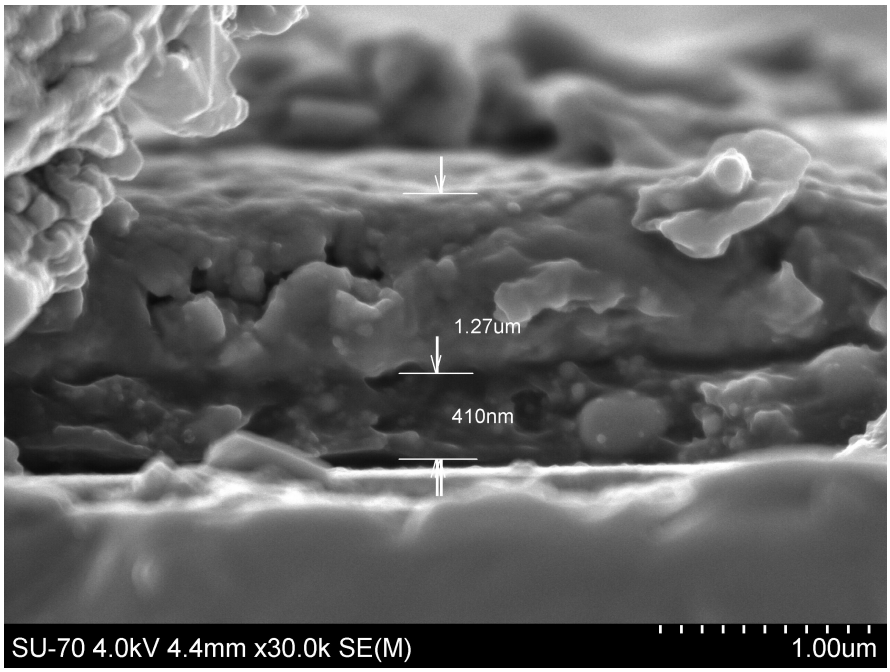

Figure 4.19: SEM cross-sections of a Si-NC/P3HT hybrid solar cell made from 2:1 (Si-NC/P3HT) wt.%. The thicknesses of the photoactive layer and Al contact are about 410 nm and 1.2 µm, respectively.

4.5.4 Current-voltage characterization of hybrid solar cells made from unetched Si-NC/P3HT with 2:1 wt.%

For comparison, we have fabricated hybrid solar cells using unetched-Si-NCs. The corresponding I-V curve is shown in Figure 4.20. No photovoltaic effect has been observed for these solar cells. The rectification factor at ±2 V was found to be 13.9, which is much higher than the value calculated for solar cells made from HF-etched Si-NCs.

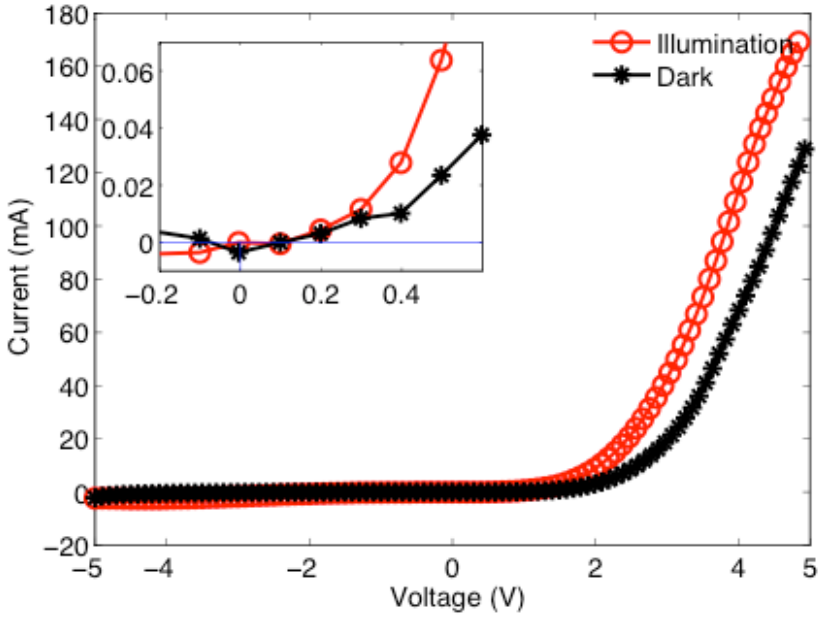

Figure 4.20: I-V curve for hybrid solar cells made from un-etched Si-NC/P3HT blend at 2:1 (Si-NCs: P3HT) wt. The inset plot shows the I-V characteristics around zero. I-V measurement was done in air under A.M 1.5 illumination and in dark.

Figure 4.21 compares air degradation of solar cells made from HF-etched and unetched Si-NCs. We monitored air degradation of the devices by measuring the I-V characteristics of the solar cells at different air exposure times and taking the current at ±4.5 V. From the figure it can be seen that, solar cells made from HF-etched Si-NCs degrade at a faster rate than solar cells made from unetched Si-NCs. This could be a result of the oxidation of HF-etched Si-NCs.

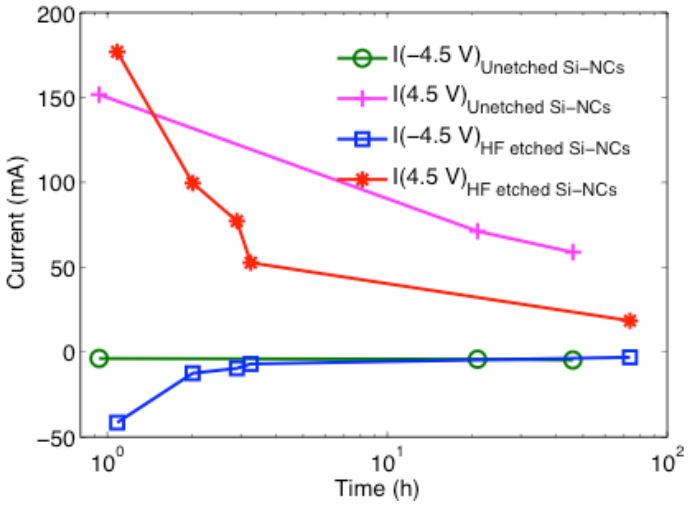

Figure 4.21: Comparison of air degradation of HF-etched/unetched Si-NC/P3HT hybrid solar cells. The current at ±4.5 V has been monitored to study the degradation of the solar cell with time.

4.5.5 Current-voltage characterization of hybrid solar cells made from Si-NC/P3HT with 2:1 wt.% (processed in nitrogen)

To investigate whether the small photovoltaic effect in the hybrid solar cells was mainly due to the fabrication of the devices in air, both the deposition and annealing of PEDOT:PSS and HF-etched Si-NCs/P3HT films were done in a nitrogen filled glove bag. Despite the use of nitrogen filled glove bag, which minimizes the effect of oxygen and humidity, the hybrid solar cells showed a very small photovoltaic effect and their I-V curves were similar to hybrid solar cells fabricated in air, Figure 4.22. From this we conclude that the fabrication of the solar cells in air was not the critical reason for the low photovoltaic effect observed for our solar cells.

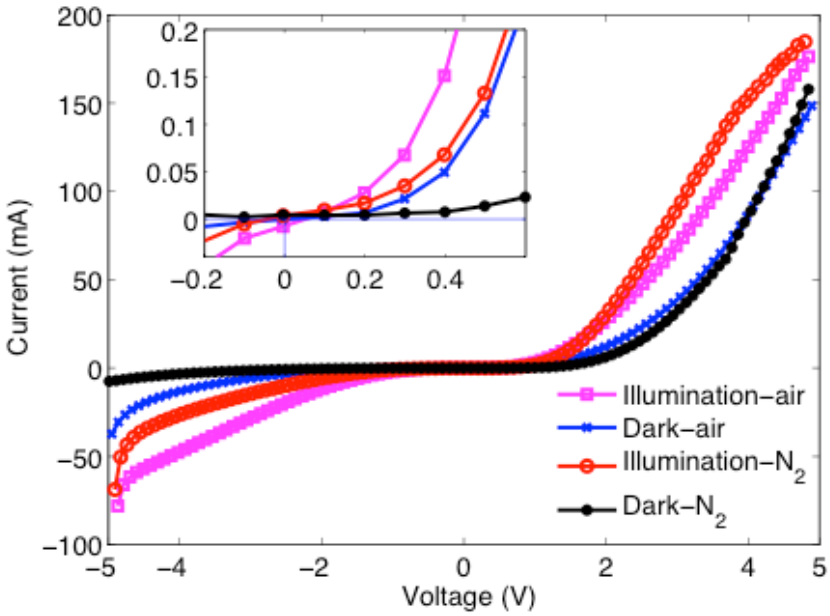

Figure 4.22: Comparison of I-V characteristics of Si-NC/P3HT hybrid solar cells fabricated in air and under N2 atmosphere. I-V measurement was done in air under A.M 1.5 illumination and in dark.

4.5.6 Discussion

One reason for the absence of photovoltaic effect in devices made from 1:1 wt.% (Si-NC/P3HT) blend could be due to the formation of insufficient interpenetrating network throughout the photoactive layer, Figure 4.8 (a) and (b), which contain Si-NC aggregates. The presence of Si-NC aggregates not only disrupt the crystallization of P3HT and hence decrease the hole mobility but also decrease the surface area of the nanocrystals decreasing the efficiency of exciton dissociation. From Figure 4.8 (a) and (b), it is evident that Si-NCs larger than 100 nm can facilitate aggregation and decrease the homogeneity of the photoactive film.

In Figure 4.8 (c) and (d) it can be clearly seen that using 2:1 wt.% of Si-NC/P3HT, resulted in improved interpenetrating network formation of Si-NCs throughout the photoactive film. As a result of this, the I-V curves for devices made from 2:1 wt.% showed higher photo and dark current values when compared to the photo and dark current values obtained for devices made from 1:1 wt.% (Si-NC/P3HT). Hence, the formation of interpenetrating network throughout the photoactive film could enhance the dissociation of excitons and transport of charge carriers to their respective electrodes.

Liu *et al.* reported that both the open circuit voltage and short circuit current decreased with increase in size of Si-NCs. Smaller Si-NCs, 3-5 nm, which have a wider bandgap of about 1.5 eV as a result of quantum confinement effect, displayed the highest open circuit voltage, 0.75 V, because of the smaller band offset between the conduction band of Si-NCs and LUMO of P3HT [9]. This decrease in band offset reduced the voltage lost during exciton dissociation and hence enhance the open circuit voltage. The highest size of Si-NCs they used was 10-20 nm, and the corresponding open circuit voltage was about 0.3 V. The maximum open circuit voltage we achieved, 0.12 V, seems consistent with their finding, as the mean diameter of Si-NCs we used was about 46.8 nm. They also obtained higher short circuit current for devices made smaller Si-NCs (3-5 nm). Larger Si-NCs can make electron-conducting path with fewer number of Si-NCs hence reduction in hoping between Si-NCs was supposed to increase the short circuit current. They argued that the achievement of small short circuit current

for larger Si-NCs could be due to the formation of bottlenecks in, P3HT, which lowers its hole conductivity and the decrease in efficiency of exciton dissociation due to decrease in surface to volume ratio of the nanocrystals.

As shown in Table 4.1, the short circuit current values obtained for our device are too small. This could be due to the presence of macroscopic aggregates, which can disturb the crystallization of P3HT and hence reduce the conductivity and reduced exciton dissociation efficiency due to decrease in surface to volume ratio of the nanocrystals, Figure 4.8 (c) and (d). To investigate whether the small photovoltaic effect in these devices is related to the fabrication of the devices in air, device fabrication was made under inert atmosphere. However, no improvement in solar cell performance has been observed. This shows that fabrication of the devices in air was not the main reason for the poor performance of the hybrid solar cells. Moreover, solar cells that exhibited a photovoltaic effect were found to degrade upon exposure to air. In contrast to this, the conductivity of P3HT, (unetched Si-NC)/P3HT and (HF-etched Si-NC)/P3HT films, studied in separate experiments, did not show significant degradation upon air exposure. These results indicate that the degradation of the solar cells is not due to degradation of individual photoactive layers, but could rather originate from degradation of interfaces between the different layers.

4.6 Electron paramagnetic resonance (EPR) measurement of HF-etched and unetched-Si-NCs

The EPR technique was found to be effective in the determination of the concentration of impurities and defects in Si-NCs [33]. The room temperature EPR spectra we recorded for unetched and HF-etched Si-NCs are shown in Figure 4.23. As shown in the figure, a computer simulation was used to decompose the EPR spectrum of unetched Si-NCs into two contributions (i) axially symmetric paramagnetic state (dotted curve) and (ii) isotropic signal (dash curve). The best fit (red solid curve) was found for g=2.0055 for isotropic resonance and $g_{\perp}$=2.0087 and $g_{//}$=2.0017 for axially symmetric defects, as it has been described in previous studies [33].

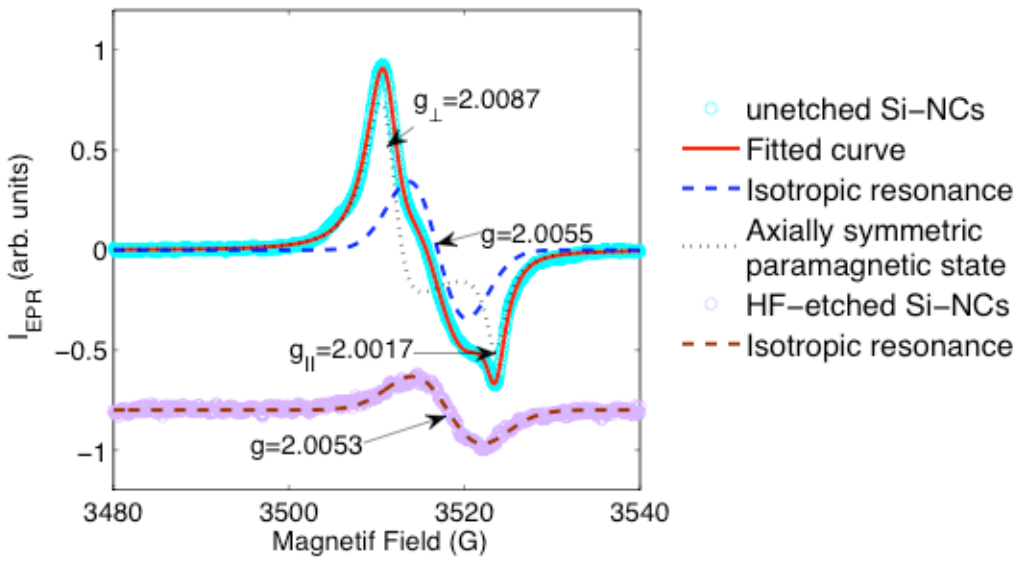

Figure 4.23: EPR spectra of un-etched Si-NCs with the fitted curved decomposed into isotropic and axially symmetric paramagnetic states and HF-etched Si-NCs where the EPR spectrum is dominated by isotropic contribution. The mean particles size of the nanocrystals used was 46.8 nm. The EPR spectrum shown for HF-etched Si-NCs was taken after exposing Si-NCs in air for 6.2 hours. Both EPR spectra were normalized to the mass of the samples. The microwave frequency was 9.8733 GHz.

While the origin of isotropic paramagnetic states are silicon dangling bonds (Si-dbs) in a disordered environment, denoted as D centers, the axial paramagnetic state originates from Si-dbs (trivalent silicon atoms) at the interface between the crystalline core of Si-NCs and the SiO_2 oxide shell, denoted as Pb-type defects. As shown in Figure 4.23, the EPR spectrum of HF-etched Si-NCs is mainly dominated by the signal from isotropic paramagnetic state, as a result of the removal of the oxide shell. The densities of defects of the two contributions were calculated from the integrated intensity of their corresponding EPR spectrum. Table 4.2 shows the total density of defects measured before and after HF etching of Si-NCs. As shown in the table, for our Si-NCs the total defect concentration after HF etching is one order of magnitude less than total defect concentration of oxidized Si-NCs due to the absence of EPR signal from axially symmetric paramagnetic states, Pb-type defects and decrease of the amount of D centers.

The average number of defects per Si-NC, which was calculated taking into account the measured intensity of defects and the Si-NCs size, are 31.6 and 3.2 for the oxidized and HF-etched Si-NCs respectively.

For comparison, we have also done EPR measurements for as grown and oxidized Si-NCs (having a mean diameter of 3 – 5 nm) from the same source as those used by Liu *et al.* [9]. As shown in Table 4.2, the amount of defects in the Si-NCs used by Liu *et al.* is much lower than the amount of defects present in our Si-NCs.

In Si-NCs, the energy states of single dangling bonds at the interface between the crystalline core of Si-NC and SiO_2 layer (energy of interfacial traps) is located in the middle of the bandgap. These trap states in Si-NCs can effectively capture photogenerated electrons and hence decrease the performance of Si-NC/P3HT hybrid solar cells. As a result, the achievement of a very small or no photovoltaic effect in our Si-NC/P3HT hybrid solar cells could be due to the higher amount of defects per particle in our Si-NCs.

Table 4.2: Density of defects and number of defects per particle for our Si-NCs before and after HF etching, and Si-NCs used in [9].

Si-NCs	Density of defects/ cm^2	Defects per Si-NCs
Unetched Si-NCs	5.19×10^{11}	31.6
HF-etched Si-NCs	5.33×10^{10}	3.2
As grown 3-5 nm Si-NCs	$(0.7 - 8.25) \times 10^{10}$	0.001 - 0.080
Oxidized 3-5 nm Si-NCs	$(0.2 - 1.5) \times 10^{11}$	0.002 - 0.143

A large increase in total defect concentration of HF-etched Si-NCs has been observed after exposing our Si-NCs to air for nearly 10 hours, Figure 4.24. Defect concentrations due to axially symmetric paramagnetic states are the ones that are strongly affected with oxidation of the nanocrystals.

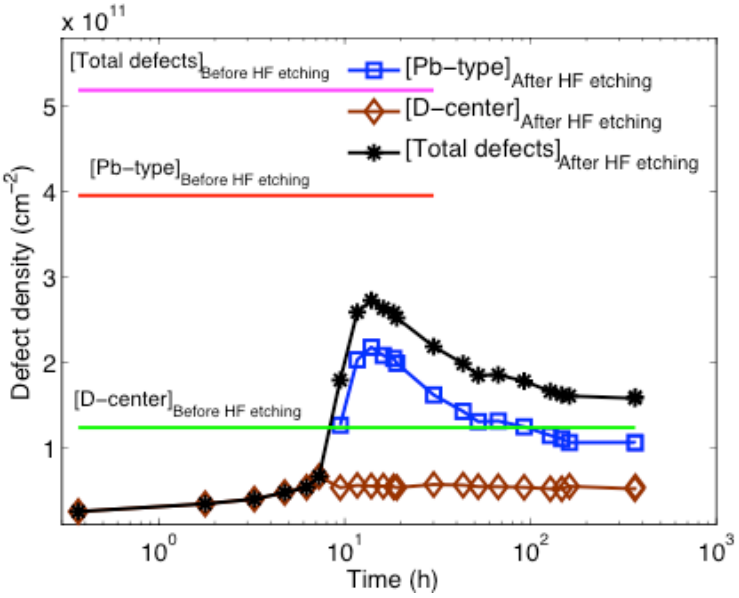

Figure 4.24: Change of isotropic defect concentration [D-center], axially symmetric defect concentration [Pb-type] with air exposure time, and total defect concentration [Pb-type + D-center] before and after HF etching of our Si-NCs. The time axis is in log scale.

Figure 4.25 compares the change of intensity of Si-O-Si FTIR absorption peak [36] and change of total defect concentration of HF-etched Si-NCs with air exposure time. As shown in the figure, a rapid increase in intensity of Si-O-Si FTIR peak and in EPR intensity of total defect concentration of HF-etched Si-NCs has been observed after exposing the Si-NCs film nearly for 10 hours.

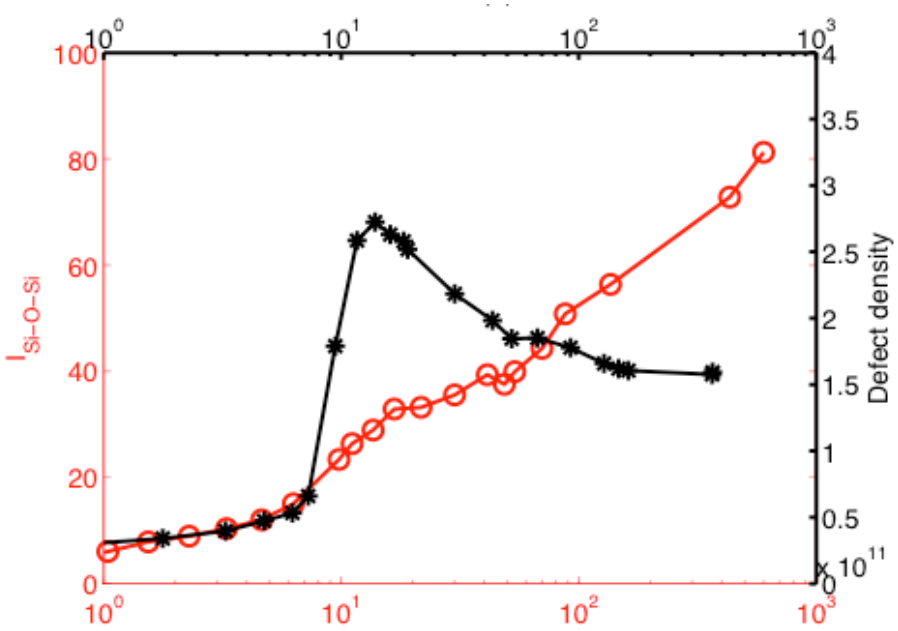

Figure 4.25: Comparison of change of Si-O-Si FTIR absorption peak intensity (red curve) and defect density (black curve) of HF-etched Si-NCs with air exposure time.

5. Conclusions and Outlook

5.1 Conclusions

Fabrication of Si-NC/P3HT hybrid solar cells under nitrogen and at ambient conditions has been carried out. Si-NCs were used in conjunction with P3HT because of their appropriate electron affinity and ionization potential differences, which are responsible for dissociation of excitons and generation of photocurrent. As a result of this, high photo- to dark- conductivity ratio has been obtained for HF-etched Si-NC/P3HT films. As a result of incorporation of Si-NCs into the polymer without sacrificing their solution processability, the transmittance (below 500 nm) of Si-NC/P3HT film is less than the transmittance of pristine P3HT film. No detectable photovoltaic effect has been observed for devices made at 1:1 wt.% (Si-NCs: P3HT). This could be due to the formation of insufficient interpenetrated network between inorganic (Si-NCs) and organic semiconductor (P3HT) phases, as confirmed by SEM. The formation of interpenetrated network was improved by increasing the concentration of Si-NCs in the blend, 2:1 wt.% (Si-NCs:P3HT). Devices made from 2:1 (HF-etched Si-NCs:P3HT) wt.% showed a photovoltaic effect. The corresponding solar cell parameters: open circuit voltage (V_{OC}) and short circuit current (I_{sc}), and power conversion efficiency (PCE) were 106 mV, 12.12 µA, and 5.1 x 10^{-5} % respectively. To study whether this very small photovoltaic effect was due to the fabrication of devices in air, device fabrication was done in a glove bag purged with nitrogen. By doing so, no improvement in solar cell performance has been found. Showing that, air processing is not the limiting factor. Moreover, the I-V characteristics of the hybrid solar cells found to degrade quickly upon air exposure. To study the performance and degradation of the solar cells in detail, the change in conductivity of P3HT, unetched Si-NC/P3HT and HF-etched Si-NC/P3HT films with air exposure time was monitored. Although the conductivity of the Si-NC/P3HT blend was less than the conductivity of pristine P3HT film, the photo- to dark conductivity ratio of the blend was higher than that of pristine P3HT film. Moreover, the photo and dark conductivity as well as photo- to dark

conductivity ratio of HF-etched Si-NC/P3HT film was higher than unetched Si-NC/P3HT film. This improvement could be due to enhanced conductivity of Si-NCs as a result of removal of the insulating SiO_2 layer and much lower concentration of defects present in HF-etched Si-NCs, as confirmed through EPR measurement. Conductivities of P3HT, unetched Si-NC/P3HT and HF-etched Si-NC/P3HT films did not show significant change for a long time upon exposure of the films to air. Hence, the rapid degradation of the solar cells is not directly related to degradation of the photoactive film. This shows that the stability of the solar cells should rather be affected by changes in the interface between the different layers in the solar cells. EPR results showed a high concentration of defects (about 32 per particle) in Si-NCs, which decreases by one order of magnitude after HF-etching. For HF-etched Si-NCs, a drastic change in defect concentration has occurred after exposing them to air for nearly 10 hours. This drastic change in defect concentration in HF-etched Si-NCs is in agreement with the increase in intensity of Si-O-Si FTIR band. The poor performance of Si-NC/P3HT hybrid solar cells could be due to high concentration of defects, as they trap photo generated electrons and hence decrease the short circuit current.

5.2 Future work

Thermal annealing could be used to reduce the concentration of defects on the surface of Si-NCs [39]. Hence the effect of varying defect concentration on the performance of Si-NC/P3HT hybrid solar cells could be studied. The morphology of the photoactive films could be optimized in order to get homogenous interpenetrated network throughout the photoactive film. Moreover, the relationship between photosensitivity losses with structural degradation of the photoactive films in air could be studied in detail.

6. Bibliography

1. Hamakawa, Y., *Solar PV energy conversion and the 21st century's civilization.* Solar Energy Materials and Solar cells, 2002. **74**: p. 13 - 23.
2. Troshin, P.A., Lyubovskaya, R. N., and Razumov, V. F., *Organic Solar Cells: Structure, Materials, Critical Characteristics, and Outlook.* Nanotechnologies in Russia, 2008. **3**: p. 242-271.
3. Ligui, L., Guanghao, L., Xiaoniu, Y., and Enle, Z., *Progress in polymer solar cell.* Chinese Science Bulletin, 2007. **52**: p. 145-158.
4. Nunzi, J.M., *Organic photovoltaic materials and devices.* C.R Physique, 2002. **3**: p. 523 - 542.
5. Ong, P.L., Levitsky, I. A. , *Organic / IV, III-V Semiconductor Hybrid Solar Cells.* Energies, 2010. **3**: p. 313-334.
6. Gur, I., Fromer, N. A., Chen, C. P, Kanaras, A. G., and Paul Alivisatos, A., *Hybrid Solar Cells with Prescribed Nanoscale Morphologies Based on Hyperbranched Semiconductor Nanocrystals.* Nano Lett., 2007. **7**(2): p. 409-414.
7. Waldo, J.E., Martijn, M. W, and René, A. J. , *Hybrid solar cells from regioregular polythiophene and ZnO nanoparticles.* Advanced Functional Materials, 2006. **16**: p. 1112-1116.
8. Hongwei, G., Qiyun, Q., Chong, C., Huan, W., and Mingtai, W., *Influence of surface mondification with carboxylic acids on the performance of polymer/titania photovoltaic devices* Journal of electronic materials, 2010. **39**(1).
9. Liu, C., Holman, Z. C., and Kortshagen, U., *Hybrid Solar Cells from P3HT and Silicon Nanocrystals.* Nano Lett., 2009. **9**: p. 449-452.
10. Benanti, T.L., and Venkataraman, D., *Organic solar cells: An overview focusing on active layer morphology.* Photosynthesis Research, 2006. **87**: p. 73-81.
11. Gratzel, M., *Dye-sensitized solar cells.* Journal of Photochemistry and Photobiology C: Photochemistry Reviews, 2003. **4**: p. 145-153.
12. Grätzel, M., *Photoelectrochemical cells.* Nature, 2001. **414**: p. 338-344.
13. Saunders, B., Turner, M., *Nanoparticle–polymer photovoltaic cells.* Advances in Colloidal Interface Science, 2008. **138**: p. 1- 23.
14. Švrček, V., Fujiwara, H., and Kondo, M., *Improved transport and photostability of poly(methoxy-ethylexyloxyphenylenevinilene) polymer thin films by boron doped freestanding silicon nanocrystals.* Applied Physics Letters, 2008. **92**(143301).
15. Liu, C.Y., Holman, Z. C., and Kortshagen, U., *Optimization of Si NC/ P3HT Hybrid Solar Cells.* Advanced Functional Materials, 2010. **20**: p. 1-8.
16. Singh, R.K., Kumar, J., Singh , R., Kant, R., Chand, S., Kumar, V., *Micromorphology, photophysical and electrical properties of pristine and ferric chloride doped poly(3-hexylthiophene) films.* Materials Chemistry and Physics, 2007. **104**: p. 390-396.
17. Li, Y., Nie, W., Liu, J., Partridge, A., and Carroll, D. L., *The Optics of Organic Photovoltaics: Fiber-Based Devices.* IEEE Journal of selected topics in quantum electronics, 2010: p. 1 - 11.

18. Yuan Li, W.N., Jiwen Liu, Ashton Partridge, and D. L. Carroll, *The Optics of Organic Photovoltaics: Fiber-Based Devices.* IEEE Journal of selected topics in quantum electronics, 2010: p. 1 - 11.
19. Tang, C.W., *Two layer organic photovoltaic cell.* Appl. Phys. Lett., 1986. **48**.
20. Unger, E.L., Ripaud, E., Leriche, P., Cravino, A., Roncali, J., Johansson, E. M. J., Hagfeldt, A., and Boschloo, G., *Bilayer Hybrid Solar Cells Based on Triphenylamine-Thienylenevinylene Dye and TiO_2.* J. Phys. Chem. C, 2010. **114**(26).
21. Gunes, S., Fritz, K., Neugebauer, H., Sariciftci, N. S., Kumar, S., Scholes, G., *Hybrid solar cells using PbS nanoparticles.* Solar Energy Materials & Solar cells, 2007. **91**: p. 420-423.
22. Greenham, N.C., Peng, X., and Alivisatos, A. P. , *Charge separation and transport in conjugated-polymer/semiconductor-nanocrystal composites studied by photoluminescence quenching and photoconductivity.* Physical Review B, 1996. **54**: p. 17628-17637.
23. Huynh, W.U., Dittmer, J.J, Paul Alivisatos, A., *Hybrid Nanorod-Polymer Solar Cells.* Science, 2002. **295**: p. 2425-2427.
24. Kumar, S., Nann, T., *First solar cells based on CdTe nanoparticle/ MEH-PPV composites.* J. Mater Res., 2004. **19**: p. 1990-1994.
25. Kumar, S., Scholes, G., *Colloidal nanocrystal solar cells.* Microchim Acta, 2008. **160**: p. 315-325.
26. Ji, L.W., Shih, W. S., Fang , T. H., Wu, C. Z., Peng, S. M., Meen, T. H., *Preparation and characteristics of hybrid ZnO-polymer solar cells.* J. Mater. Sci., 2010. **45**: p. 3266-3269.
27. Xiang, H., and Wei, S. H., *Identifying Optimal Inorganic Nanomaterials for Hybrid Solar Cells.* J. Phys. Chem. C, 2009. **113**: p. 18968-18972.
28. Delerue, C., Allan, G. , and Lannoo, M., *Theoretical aspects of luminescence of porous silicon.* Physical Review B, 1993. **48**: p. 11024 - 11036.
29. Knipping, J., Wiggers, H., Rellinghaus, B., Roth, P., Konjhodzic, D., and Meier, C., *Synthesis of High Purity Silicon Nanoparticles in a Low Pressure Microwave Reactor.* J. Nanosci. Nanotech., 2004. **4**: p. 1039-1044.
30. Bruno, G., Capezzuto, P., and Cicala, G., *Chemistry of Amorphous Silicon Deposition Processes: Fundamentals and Controversial Aspects*, in *Plasma Deposition of Amorphous Silicon-Based Materials*, P.C. Giovanni Bruno, Arun Madan, Editor. 1995, Academic Press.
31. Jeffries-El, M., and McCullough, R. D., *Conjugated polymers theory, synthesis, properties, and characterization*, in *regioregular polythiophenes*, T.A.S.a.J.R. Reynolds, Editor. 2007, CRC Press, Taylor & Francis Group.
32. Reyes, M., Kim, K., and Carroll, D., *High-efficiency photovoltaic devices based on annealed poly(3-hexylthiophene) and 1-(3-methoxycarbonyl)-propyl-1- phenyl-(6,6) C_{61} blends.* Applied Physics Letters, 2005. **87**(083506).
33. Pereira, R.N., Stegner, A.R., Klein, K., Lechner, R., Dietmueller,R., Wiggers, H., Brandt, M.S., Stutzmann, M. , *Electronic transport through Si nanocrystal films: Spin-dependent conductivity studies.* Physica B, 2007. **401 -402**: p. 527 -530.
34. Theiβ, W., *Optical properties of porous silicon.* Surface science reports, 1997. **29**: p. 91-192.
35. Retrieved from: http://en.wikipedia.org/wiki/Solar_cell#Equivalent_circuit_of_a_solar_cell, 2010

36. You, W., *Electrical properties of Si nanocrystal films processed from Si-inks*, in *Material Science, Thesis*. 2009, University of Aveiro: Aveiro. p. 60.
37. Chang, Y.M., *Influence of photo-induced degradation on the optoelectronic properties of regioregular poly(3-hexylthiophene).* Solar energy materials and solar cells, 2008. **92**: p. 761-765.
38. Hoppe, H., and Sariciftci, N.S., *Morphology of polymer/fullerene bulk heterojunction solar cells.* J. Mater. Chem., 2006. **16**: p. 45-61.
39. Niesar, S., Stegner, A. R., Pereira, R. N., Hoeb, M., Wiggers, H., Brandt, M. S., and Stutzmann, M., *Defect reduction in silicon nanoparticles by low-temperature vacuum annealing.* Applied Physics letters, 2010. **96**(193112).